



## RESEARCH ARTICLE

10.1029/2021GC009805

### Special Section:

Slow Slip Phenomena and  
Plate Boundary Processes

### Key Points:

- E-verging thrusting at blueschist facies conditions affects the basement of the Northern Apennines and preserves brittle/ductile structures
- During subduction local dehydration reactions triggered transiently high pore pressure in continental metasediments at ~1.1 GPa and 350°C
- Coeval carpholite dilational shear veins and mylonitic foliation can be a geological record of deep episodic tremor and slow slip events

### Supporting Information:

Supporting Information may be found in the online version of this article.

### Correspondence to:

F. Giuntoli,  
[francesco.giuntoli@unibo.it](mailto:francesco.giuntoli@unibo.it)

### Citation:

Giuntoli, F., & Viola, G. (2021). Cyclic brittle-ductile oscillations recorded in exhumed high-pressure continental units: A record of deep episodic tremor and slow slip events in the Northern Apennines. *Geochemistry, Geophysics, Geosystems*, 22, e2021GC009805. <https://doi.org/10.1029/2021GC009805>

Received 22 MAR 2021

Accepted 18 AUG 2021

# Cyclic Brittle-Ductile Oscillations Recorded in Exhumed High-Pressure Continental Units: A Record of Deep Episodic Tremor and Slow Slip Events in the Northern Apennines

Francesco Giuntoli<sup>1</sup>  and Giulio Viola<sup>1</sup> 

<sup>1</sup>Department of Biological, Geological, and Environmental Sciences, Università degli Studi di Bologna, Bologna, Italy

**Abstract** The geological record of deep fossil seismogenesis in subduction zones is limited due to common rock overprinting during exhumation and only a few regions expose well-preserved deeply exhumed structures. We investigated a mesoscopic contractional duplex formed at blueschist facies conditions in continental metasediments in the Northern Apennines (Italy). Field observations reveal strain partitioning within the duplex between metapelite bands, corresponding to high-strain zones, and metaquartzarenite bands, which form low-strain, imbricated metric horses. Dilational shear veins occur in both lithotypes and are composed of quartz and carpholite fibers defining a stretching lineation parallel to the regional SW-NE transport direction. Geometrical, cross cutting and petrographic relationships suggest that veins formed broadly syn-mylonitization. Thermodynamic modeling constrains the formation of the mylonitic foliation to >0.7 GPa and ~400°C and the dilational shear veins vein to ~1.1 GPa and 350°C. Therefore, we document a top-to-the-E-NE thrust that formed at the deepest conditions recorded by this unit of the Northern Apennines. In the thrust continental metasediments, aqueous fluid locally released by metamorphic dehydration reactions transiently increased pore pressure, in turn triggering brittle-ductile cyclicality. We propose that blueschist facies dilational shear veins and mylonitic foliation represent a geological record of deep episodic tremor and slow slip events. To the best of our knowledge, this is the first time that these events are genetically associated with brittle and ductile structures of a mesoscopic duplex. We suggest that these structures could be common features of the high-pressure metamorphic units of the Apennine orogenic belt.

**Plain Language Summary** The rock record of deep seismic activity is scanty because subducted rocks commonly reequilibrate during exhumation enroute to the surface. The Italian Northern Apennines expose deeply subducted rocks exhumed back to the surface that still preserve deep mineralogical assemblages and structures. We studied a contractional structure (thrust) deforming metamorphosed Palaeozoic continental sediments. These rocks display evidence of coeval discontinuous and continuous deformation in the form of veins and foliation planes, respectively. By using mineralogical assemblages and thermodynamic modeling, we constrain the formation of both veins and foliation to pressure and temperature conditions of ~1 GPa and 350°C. These results suggest depths of 30–40 km and cold geothermal gradients typical of subduction zones. We propose that episodic pulses of aqueous fluids released due to destabilization of hydrated minerals during subduction is responsible for the formation of the observed veins. We suggest that these geological structures can be regarded as a fingerprint of deep episodic tremor and slow slip events, peculiar seismic phenomena commonly indirectly documented at convergent margins by geophysical and geodetic techniques.

## 1. Introduction

Structures and parageneses typical of deeply subducted units that form at high-pressure (HP) conditions are scanty in the geological record because they are commonly overprinted, and thus partly or fully obliterated along their exhumation path by younger fabrics and/or metamorphic reequilibration. Whenever possible, their identification and comprehensive characterization are, therefore, of great importance when aiming at reconstructing deep tectono-metamorphic processes in subduction zones. Interestingly, brittle and ductile deformation styles have been shown to alternate and repeat cyclically at comparable pressure-temperature

© 2021. The Authors.

This is an open access article under the terms of the [Creative Commons Attribution License](https://creativecommons.org/licenses/by/4.0/), which permits use, distribution and reproduction in any medium, provided the original work is properly cited.

(P-T) conditions in several deeply subducted units, which has noteworthy implications upon the deep seismic cycle and subduction dynamics (e.g. Angiboust et al., 2012; Austrheim, 1987; Giuntoli, Brovarone, et al., 2020; Molli et al., 2017). This transient cyclic behavior is triggered and steered by the interplay of different chemical and physical parameters, including, but not limited to, strain rate and stress variations, pore pressure fluctuations between hydro- and lithostatic conditions, mineral reactions, and associated strain weakening or hardening of the deforming rock (Brander et al., 2012; Bukovská et al., 2016; Gerald & Stünitz, 1993; Giuntoli, Menegon, et al., 2020; Gueydan et al., 2003; Hyndman, 1994; Mancktelow & Pennacchioni, 2005; Marchesini et al., 2019; Menegon & Fagereng, 2021; Menegon et al., 2013; Prando et al., 2020; Putnis, 2015; Simpson, 1986; Torgersen & Viola, 2014; Viola et al., 2006; Wehrens et al., 2016).

In the last decades, episodic tremor and slow slip events (ETS) have been documented worldwide in several active subduction settings (Dragert et al., 2001; Obara, 2002; Shelly et al., 2006). Tremors are a persistent low-frequency seismic signal associated with slow slip, a geodetically detected slip larger than the average plate motion (e.g. Behr & Bürgmann, 2021; Beroza & Ide, 2011; Gombert et al., 2010; Ito et al., 2007). Their seismological signature is characterized by high  $V_p/V_s$  ratios, where pore pressure may transiently reach and even exceed lithostatic values (e.g., Bernaudin & Gueydan, 2018; Saffer & Tobin, 2011). Recently, field-based studies have proposed broadly coeval brittle and ductile deformation features to be the physical expression of ETS (Angiboust et al., 2015; Barnes et al., 2020; Behr et al., 2018; Compton et al., 2017; Kotowski & Behr, 2019; Molli et al., 2017; Muñoz-Montecinos et al., 2020; Tarling et al., 2019). Notably, dilational shear veins (referred to as “dilational hydroshears” by Fagereng et al., 2010) in shallow subduction settings are currently considered as one key, diagnostic element of the geological record of episodic tremor and slow slip events (ETS; Fagereng et al., 2011). However, further characterization is needed to link these microscopic structures to meso- and macroscopic structures and to unravel the details of the deformation mechanisms and mineral reactions occurring during subduction at seismogenic depths (Behr & Bürgmann, 2021; Kirkpatrick et al., 2021).

The Northern Apennines orogenic belt of Italy (NA) represents a natural laboratory to study exhumed structures originally formed at HP conditions aiming to unravel their tectonometamorphic history and seismogenic role. Here, we present the results of the study of a thrust in the NA and an associated ~30 m long contractional duplex. The duplex is formed by little deformed metaquartzarenite horses that are imbricated along higher strain zones localized along metapelite layers. Dilational hydroshear veins are common throughout. By field and microstructural analysis integrated with thermodynamic modeling and compositional X-ray mapping, we document that both mylonitic foliation and brittle dilational hydroshear veins formed broadly coevally during the Apennine orogeny at HP conditions corresponding to 30–40 km depth in the W-dipping subduction channel. We suggest that the thrust represents one of the deepest structures preserved in the Northern Apennines and that it is kinematically associated with the general E-NE vergence of the belt. We conclude that the documented fabrics formed by cyclic brittle-ductile deformation, likely triggered by fluctuating pore pressure due to metamorphic dehydration reactions. Moreover, we propose that they can represent a geological record of deep ETS in the NA fossil and exhumed subduction channel. Additionally, we speculate that this blueschist facies thrust may be correlated with blueschist fabrics described on Elba Island that record the opposite, top-to-the W, sense of shear (Ryan et al., 2021), although further geochronological work is needed to test that structures are coeval. Elaborating on this possible correlation, we offer further evidence that the initial and deepest exhumation of the HP units of the NA was synorogenic and that it may have occurred in the kinematic framework of an extruding wedge system during overall compression.

## 2. Geological Setting

The Apennines formed due to the convergence between and successive collision of the European and African plates from the Late Eocene (e.g., Carminati & Doglioni, 2012; Molli, 2008; Vignaroli et al., 2009, Figure 1). The innermost NA offer the opportunity to study a unique setting made of oceanic and continental units that were subducted to high pressure-low temperature conditions (HP-LT) comprised between 0.8–1.6 GPa and 300°C–500°C (Ligurian and Tuscan Metamorphic Units, respectively; summary of P-T and age data in Figure 1 of Bianco et al., 2019 and references therein). Successively, these tectonic units were exhumed, stacked, and juxtaposed below their nonmetamorphic counterparts (Ligurian Units and Tuscan

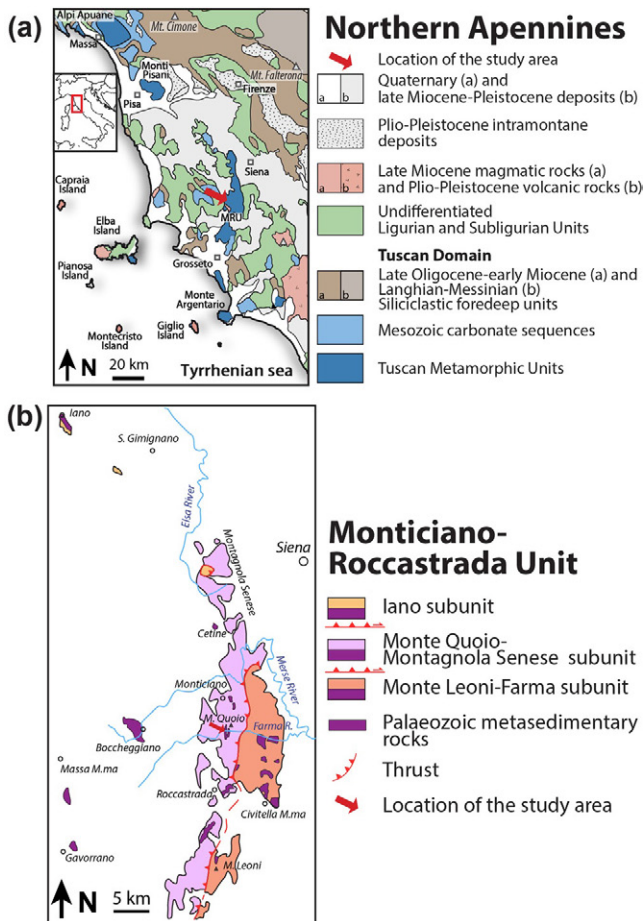


**Figure 1.** (a) Geological setting of the Northern Apennines. MRU: Monticiano-Roccastrada Unit. (b) Tectonic map of the Monticiano-Roccastrada Unit highlighting the three tectonic subunits and the location of the study area. Modified from Brogi and Giorgetti (2012) and Lazzarotto et al. (2003).

Nappe). In the NA, only few structures are directly related to HP parageneses (Monticiano-Roccastrada Unit: Brogi & Giorgetti, 2012; Massa Unit: Molli et al., 2000; some evidence for the Acquadolce Subunit, Elba Island: Ryan et al., 2021), whereas most of the preserved ductile structures are defined by greenschist facies retrograde assemblages, with the relic HP parageneses only preserved in microlithons (Monte Argentario: Theye et al., 1997; Elba Island: Bianco et al., 2019; Papeschi et al., 2020; Monti Pisani: Lo Pò & Braga, 2014).

We studied a well exposed section in the Monticiano-Roccastrada Unit (MRU) of the Mid Tuscan Ridge (Figure 1). The MRU is internally subdivided by c. N-S trending thrusts into the Iano-, the Monte Quoio-Montagnola Senese- and the Monte Leoni-Farma subunits (from structurally higher to lower and from internal to external; Figure 1, Costantini et al., 1988; Lazzarotto et al., 2003). The Monte Quoio-Montagnola Senese subunit is well exposed along the Farma River, where it appears to be composed of three metasedimentary formations, which, from oldest to the youngest, are: (a) the Risanguigno Formation (Lower Devonian based on Lazzarotto et al., 2003 and references therein; Middle Mississippian according to Capezzuoli et al., 2021), consisting of marine deposits comprising black phyllite intercalated with dolostone beds, radiolarian chert, green metasandstone, and quartzitic phyllite; (b) the Arenarie di Poggio al Carpino Formation (Late Permian-Early Triassic), the target of this study, which is composed of quartz-rich metasandstone, metaconglomerate, and minor metapelite deposited in shallow marine, inner shelf environments and shore deposits; (c) the Civitella Formation comprising green-gray metasandstone intercalated with lenses of metaconglomerate deposited in an alluvial fan system and belonging to the Verrucano Group (Lower-Middle Triassic; details and references in Aldinucci et al., 2008; Casini et al., 2008; Conti et al., 1991; Lazzarotto et al., 2003).

A mesoscopic contractional duplex deforms the Palaeozoic-Triassic quartz-rich metasandstones, metaconglomerates and minor metapelites of the Arenarie di Poggio al Carpino Formation. This structure is described in detail in Casini et al. (2007 and 2008); a detailed structural map is available in Figures 4 and 5 of Casini et al., 2008). The more competent metarenite defines the duplex horses, each a few meters thick and enveloped by an up to one meter thick metapelite layer. Veins occur within the roof and floor thrusts and the connecting splays and contain quartz fibers that define a penetrative stretching lineation oriented W/SW-E/NE and plunging gently in both directions. Kinematic indicators constrain an overall top-to-the-E/NE sense of shear. No metamorphic minerals were reported associated with this structure, which has been traditionally interpreted as a series of metric boudins representing an extensional pre-Apenninic structural feature that became inverted during the Apennine orogeny to form the duplex associated with a E/NE-vergent thrust (Casini et al., 2007, 2008).

Carpholite is a blueschist facies index mineral of metasedimentary rocks (e.g. Agard et al., 2005; Black et al., 1993; Bousquet et al., 1998; El-Shazly, 1995; Goffé & Oberhänsli, 1992; Rimmelé et al., 2003; Viswanathan & Seidel, 1979). Carpholite is reported in the NA from the Verrucano Formation of the MRU, the Monte Argentario, and Giglio Island (Brogi & Giorgetti, 2012; Capponi et al., 1997; Giorgetti et al., 1998; Rossetti et al., 1999; Theye et al., 1997). However, carpholite therefrom is mostly preserved as mineral relics in microlithons and it does not mark any penetrative fabric, with a few exceptions (Brogi & Giorgetti, 2012). Evidence of several metamorphic and deformation stages is reported from the Verrucano Formation of the MRU, where isoclinal folds are reported to have initially formed leading to the development of an axial planar composite foliation (i.e., bedding + metamorphic foliation) under blueschist facies conditions ( $P \geq 1.1$  GPa and  $T$  370°C–420°C; Monte Quoio-Montagnola Senese subunit; Brogi & Giorgetti, 2012; Conti

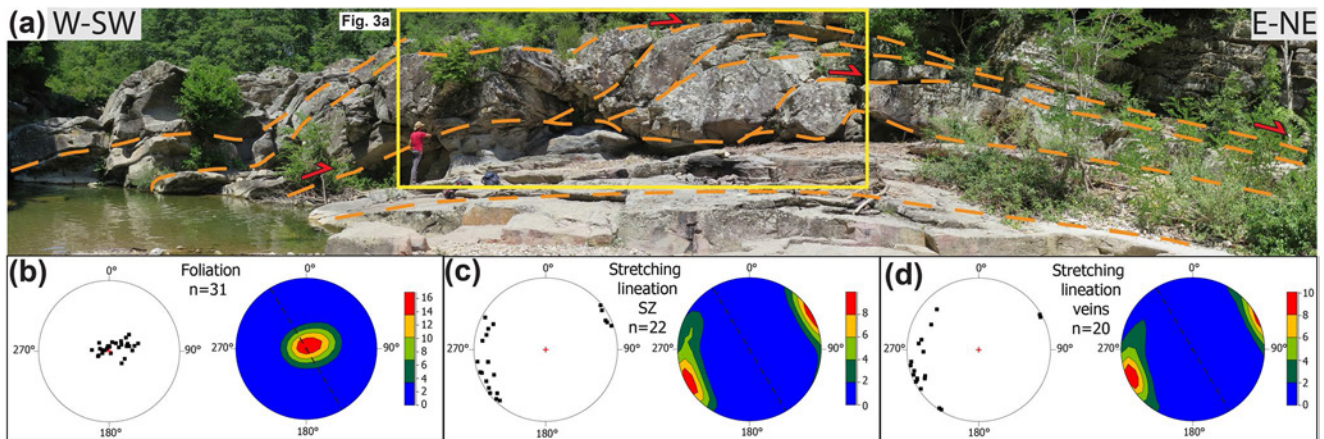


**Figure 2.** (a) Mesoscopic duplex along the Farma River at the locality “I Canaloni.” The dashed orange lines highlight some of its horses and the trend of the composite foliation, the arrows the sense of shear. The entire duplex is deformed by an open fold with subhorizontal axis and subvertical axial plane trending NNW-SSE (dashed black line in the stereoplots). (b) Stereographic plot of poles to mylonitic foliation planes within horse-bounding high-strain shear zones. (c and d) Stretching lineation in metapelite and metaquartzarenite, and in veins, respectively. Equal area, lower hemisphere projections (Stereo 32 software). Data from this study and from Casini et al. (2008).

et al., 1991; Costantini et al., 1988). Two generations of quartz-carpholite veins have been recognized and interpreted as broadly coeval with this composite foliation (Brogi & Giorgetti, 2012). These veins infill tension gashes arranged in en-échelon arrays, with the first generation carpholite growing perpendicular to the vein walls and parallel to their opening direction. The second generation has been shown to grow at the interface between veins and host-rock and defines the local stretching lineation. These veins were linked to progressive noncoaxial deformation in brittle-ductile shear zones deforming the MRU (Brogi & Giorgetti, 2012). A younger, W-verging, and E-facing folding episode is considered responsible for the formation of a spaced discontinuous crenulation cleavage, which is more pervasive in the metapelite than in the metarenite. A later subvertical and discontinuous foliation is visible only in the metapelite and is possibly linked to regional, NNW-SSE oriented open and upright folds associated with the Mid Tuscan Ridge (Figure 2).

### 3. Material and Methods

Our approach integrates detailed fieldwork with microstructural and petrological investigations to describe the sequence of visible tectonometamorphic stages and to derive from those P-T constraints on the conditions of their formation. Thin sections were prepared from representative samples and cut as XZ sections of the strain ellipsoid parallel to the stretching lineation ( $X = L_s$  in figures) and perpendicular to the foliation ( $Z$  parallel to the pole to the foliation). In the following, we describe in detail the analytical techniques that we relied on during this study.

#### 3.1. Electron Probe Microanalyzer (EPMA) and X-Ray Compositional Map Elaboration

EPMA analysis was performed on carbon-coated thin sections using a JEOL JXA-8200 electron microprobe at the Department of Earth Sciences of the University of Milano (Italy). Backscattered electron images (BSE) were acquired using an accelerating voltage of 15 KeV, a beam current of 5 nA, and a working distance of 11 mm. Point analyses and X-ray compositional maps were acquired using wavelength-dispersive spectrometers. Point analyses were acquired before the acquisition of X-ray compositional maps on the same area. Analytical conditions of point analysis were a 15 KeV accelerating voltage, a 5 nA beam current and a beam  $\phi$  of  $\sim 1 \mu\text{m}$ . Nine oxide compositions were measured, using the following standards: grossular ( $\text{SiO}_2/\text{Al}_2\text{O}_3/\text{CaO}$ ), fayalite (FeO), forsterite (MgO), K-feldspar ( $\text{K}_2\text{O}$ ), omphacite ( $\text{Na}_2\text{O}$ ), ilmenite ( $\text{TiO}_2$ ), and rhodochrosite (MnO). Analytical conditions for X-ray map acquisition were a 15 KeV accelerating voltage, a 100 nA specimen current, and 50 ms dwell times. Nine elements (Si, Ti, Al, Fe, Mn, Mg, Na, Ca, and K)

were measured at the specific wavelength in two passes. X-ray maps were processed using XMapTools (Lanari et al., 2014) and intensity X-ray maps were standardized to concentration maps of oxide weight percentage using spot analyses as the internal standard.

### 3.2. Thermodynamic Modeling

The Gibbs free energy minimization algorithm Theriak-Domino (de Capitani & Petrakakis, 2010) was used to compute isochemical equilibrium phase diagrams, mineral isopleths, and diagrams of H<sub>2</sub>O content in solids and modal amount of the hydrous mineral phases. The thermodynamic database of Pourteau et al. (2014), based on Berman (1988) was used (Table S1). All Gibbs free energy minimizations were computed with an excess in pure H<sub>2</sub>O fluid. Local bulk compositions were obtained using standardized X-ray maps, following the procedure described in Lanari and Engi (2017). Fe<sup>3+</sup> was ignored because of its very low content or complete absence in the studied mineral phases (Table 1). Ca and Mn were removed from the input composition because of their minor content (Table S2). Plots of volume percent (vol%) of the hydrous mineral phases and weight percent (wt%) of H<sub>2</sub>O in mineral phases were computed along a prograde P-T path valid for the Northern Apennines, based on data from this study and Bianco et al. (2019).

## 4. Results

### 4.1. Mesostrucutural Analysis

We studied a section of the Farma River at the locality “I Canaloni,” where river erosion and carving allow good exposure. There, an E-W striking, ~30 m long and 5 m high contractional duplex is well exposed along the riverbank (Casini et al., 2007, 2008). Strain partitioning occurs within the duplex between metapelitic layers, corresponding to 30–100 cm thick high-strain zones, and metaquartzarenite blocks and bands, which form either relatively low-strain metric horses or 10–20 cm thick, high-strain zones separating adjacent horses (Figures 2–4). The metapelite is gray to bluish in color and is affected by a pervasive mylonitic foliation defined by quartz- and phyllosilicate-rich layers (Figure 3d; see also the detailed description of the metamorphic foliation in the next section). A stretching lineation defined by quartz and phyllosilicates is visible on the foliation planes. Foliation and stretching lineation dips and plunges gently to the W-SW (stereonet in Figures 2b and 2c and Figure 5 of Casini et al., 2007 and Figure 3 of Casini et al., 2008). The metaquartzarenite exhibits a yellow to light gray color and contains grain size variations subparallel to the metamorphic foliation, with lenses and bands of metaconglomerate, a few meters thick, composed of quartz and metapelite clasts wrapped by phyllosilicate-rich layers (stereonet in Figure 2b; Figures 3b and 3c). Therefore, the main foliation visible in the field is a composite fabric, resulting from the transposition of the original bedding and its parallelization to the metamorphic foliation. A strain gradient is visible between the horses and toward the base of the duplex along the basal thrust, where the foliation becomes mylonitic (Figures 3c, 3f, 3d, and 3g, respectively).

Veins are common features at the outcrop and represent ~1–2 vol% thereof. Veins are more abundant close to the metapelite-metaquartzarenite contact. In the metapelite, veins are subparallel to the foliation and are up to 1 m long and up to a few dm thick. Phyllosilicate-rich layers occur as inclusions and are oriented parallel to the foliation (Figure 4b). These veins are fully concordant with the foliation, similar to what reported by Koehn and Passchier (2000). In the metaquartzarenite, veins are, instead, either highly oblique to the foliation forming extension veins or parallel to the foliation only in its most sheared domains, close to the highly sheared metapelites (Figures 3b and 4b). Extension veins in the metaquartzarenite are up to one dm thick and a few dm long and are thicker close to the foliation parallel veins and taper in the host-rock, similar to what described by Koehn and Passchier (2000).

Extension veins in the metaquartzarenite are genetically associated and coeval with the foliation parallel veins, as shown by the fact that, where these intersect, no consistent crosscutting relations are observed (red arrows in Figures 3b and 4b), similar to the striped-bedding veins of Koehn and Passchier (2000) and dilational hydroshears of Fagereng et al. (2010). Koehn and Passchier (2000) suggest that variable displacement rates occurring along their striped-bedding veins induced local extension in the wall-rock and the formation of extension veins at high angle to the foliation, similar to horsetail cracks in Ohlmacher and Aydin (1997).

**Table 1**  
Representative Average Composition Analyses (wt%) of the Mineral Phases

| Sample                         | Cld           |          |                     |          |              |          | Car           |          |              |          | Ms           |          |             |          |  |  |
|--------------------------------|---------------|----------|---------------------|----------|--------------|----------|---------------|----------|--------------|----------|--------------|----------|-------------|----------|--|--|
|                                | Metapelite    |          |                     |          |              |          | Vein          |          |              |          | Metapelite   |          |             |          |  |  |
|                                | Perp. to fol. |          | Small angle to fol. |          | Par. to fol. |          | High $X_{Mg}$ |          | Low $X_{Mg}$ |          | High Si apfu |          | Low Si apfu |          |  |  |
| Wt%                            | Av Comp       | $\sigma$ | Av Comp             | $\sigma$ | Av Comp      | $\sigma$ | Av Comp       | $\sigma$ | Av Comp      | $\sigma$ | Av Comp      | $\sigma$ | Av Comp     | $\sigma$ |  |  |
| SiO <sub>2</sub>               | 25.14         | 1.41     | 24.95               | 1.15     | 24.04        | 1.43     | 39.40         | 1.40     | 40.53        | 1.57     | 48.80        | 1.16     | 45.08       | 1.35     |  |  |
| TiO <sub>2</sub>               | 0.07          | 0.03     | 0.08                | 0.10     | 0.08         | 0.03     | 0.16          | 0.06     | 0.19         | 0.06     | 0.28         | 0.22     | 0.14        | 0.05     |  |  |
| Al <sub>2</sub> O <sub>3</sub> | 43.29         | 0.87     | 43.51               | 0.90     | 43.83        | 0.82     | 33.92         | 0.90     | 33.20        | 0.87     | 34.85        | 1.43     | 35.98       | 0.91     |  |  |
| FeO                            | 24.46         | 0.80     | 23.53               | 0.90     | 23.36        | 0.65     | 8.10          | 0.61     | 8.90         | 0.60     | 0.55         | 0.27     | 0.86        | 0.16     |  |  |
| MnO                            | 0.20          | 0.07     | 0.19                | 0.06     | 0.20         | 0.08     | 0.08          | 0.04     | 0.09         | 0.04     | 0.04         | 0.02     | 0.04        | 0.02     |  |  |
| MgO                            | 3.17          | 0.37     | 3.53                | 0.32     | 3.67         | 0.34     | 8.01          | 0.48     | 7.64         | 0.46     | 0.75         | 0.15     | 0.58        | 0.16     |  |  |
| CaO                            | 0.01          | 0.00     | 0.01                | 0.00     | 0.01         | 0.00     | 0.03          | 0.03     | 0.03         | 0.03     | 0.06         | 0.02     | 0.05        | 0.01     |  |  |
| Na <sub>2</sub> O              | 0.02          | 0.02     | 0.02                | 0.02     | 0.04         | 0.03     | 0.00          | 0.00     | 0.00         | 0.00     | 1.27         | 0.25     | 0.50        | 0.34     |  |  |
| K <sub>2</sub> O               | 0.03          | 0.01     | 0.03                | 0.01     | 0.07         | 0.03     | 0.01          | 0.02     | 0.01         | 0.02     | 8.94         | 0.63     | 11.02       | 0.70     |  |  |
| CO <sub>2</sub>                | –             | –        | –                   | –        | –            | –        | –             | –        | –            | –        | –            | –        | –           | –        |  |  |
| Total                          | 96.39         | –        | 95.85               | –        | 95.29        | –        | 89.72         | –        | 90.60        | –        | 95.54        | –        | 94.24       | –        |  |  |
| Formulae based on              | on 12 O       |          |                     |          | on 8 O       |          |               |          | on 8 O       |          |              |          | on 11 O     |          |  |  |
| Si                             | 1.98          | 0.08     | 1.97                | 0.07     | 1.90         | 0.08     | 2.00          | 0.04     | 2.04         | 0.04     | 3.20         | 0.06     | 3.04        | 0.05     |  |  |
| Ti                             | 0.00          | 0.00     | 0.00                | 0.00     | 0.00         | 0.00     | 0.01          | 0.00     | 0.01         | 0.00     | 0.01         | 0.00     | 0.01        | 0.00     |  |  |
| Al                             | 4.02          | 0.09     | 4.05                | 0.08     | 4.09         | 0.09     | 2.03          | 0.05     | 1.97         | 0.05     | 2.69         | 0.09     | 2.86        | 0.08     |  |  |
| Fe <sup>3+</sup>               | 0.01          | 0.00     | 0.01                | 0.00     | 0.09         | 0.00     | 0.00          | 0.00     | 0.00         | 0.00     | 0.00         | 0.00     | 0.00        | 0.00     |  |  |
| Fe <sup>2+</sup>               | 1.60          | 0.06     | 1.54                | 0.06     | 1.46         | 0.05     | 0.34          | 0.03     | 0.38         | 0.03     | 0.03         | 0.01     | 0.05        | 0.01     |  |  |
| Mn                             | 0.01          | 0.01     | 0.01                | 0.00     | 0.01         | 0.01     | 0.00          | 0.00     | 0.00         | 0.00     | 0.00         | 0.00     | 0.00        | 0.00     |  |  |
| Mg                             | 0.37          | 0.04     | 0.41                | 0.04     | 0.43         | 0.04     | 0.61          | 0.04     | 0.57         | 0.03     | 0.07         | 0.04     | 0.06        | 0.03     |  |  |
| Ca                             | –             | –        | –                   | –        | –            | –        | –             | –        | –            | –        | 0.00         | 0.00     | 0.00        | 0.00     |  |  |
| Na                             | –             | –        | –                   | –        | –            | –        | –             | –        | –            | –        | 0.16         | 0.03     | 0.06        | 0.04     |  |  |
| K                              | –             | –        | –                   | –        | –            | –        | –             | –        | –            | –        | 0.75         | 0.05     | 0.95        | 0.06     |  |  |
| Σ cation                       | 8.00          | –        | 8.00                | –        | 8.00         | –        | 4.98          | –        | 4.97         | –        | 6.92         | –        | 7.03        | –        |  |  |
| $X_{Mg}$                       | 0.19          | 0.02     | 0.21                | 0.02     | 0.22         | 0.02     | 0.64          | 0.02     | 0.60         | 0.02     | 0.70         | 0.12     | 0.54        | 0.09     |  |  |

Note. Fe<sup>3+</sup> and Fe<sup>2+</sup> contents of carpholite following Droop (1987). Fe<sup>3+</sup> and Fe<sup>2+</sup> contents of muscovite calculated assuming full tetrahedral site occupancy.

Given these analogies and the microstructural details reported in the next section, in the following we refer to foliation parallel veins as dilational hydroshear veins (Fagereng et al., 2010).

Some veins are deformed by noncylindrical folds lengthened parallel to the metapelitic high-strain shear zones (green dashed line in Figure 4b). Later quartz veins, a few m long and few cm thick (green arrow in Figure 4c), cut at high angle both the foliation and the veins that we describe in this study. These veins will not be discussed any further, as they document a later deformation stage that is unrelated to the story discussed in here.

The entire duplex is deformed by a decametric open fold with subhorizontal axis and subvertical NNW-SSE-trending axial plane, which is associated with the regional antiform of the Mid Tuscan Ridge (Casini et al., 2007; black dashed line in the stereonet of Figure 2).

| Vein         |          |             |          | Prl        |          |         |          | Cb         |          |         |          |
|--------------|----------|-------------|----------|------------|----------|---------|----------|------------|----------|---------|----------|
| High Si apfu |          | Low Si apfu |          | Metapelite |          | Vein    |          | Metapelite |          |         |          |
| Av Comp      | $\sigma$ | Av Comp     | $\sigma$ | Av Comp    | $\sigma$ | Av Comp | $\sigma$ | Core       |          | Rim     |          |
| Av Comp      | $\sigma$ | Av Comp     | $\sigma$ | Av Comp    | $\sigma$ | Av Comp | $\sigma$ | Av Comp    | $\sigma$ | Av Comp | $\sigma$ |
| 47.97        | 1.27     | 46.63       | 1.57     | 68.79      | 1.65     | 66.92   | 1.75     | -          | -        | -       | -        |
| 0.10         | 0.04     | 0.10        | 0.06     | 0.00       | 0.00     | 0.02    | 0.02     | -          | -        | -       | -        |
| 36.03        | 1.29     | 37.35       | 1.08     | 28.55      | 0.92     | 29.76   | 0.73     | -          | -        | -       | -        |
| 0.49         | 0.18     | 0.31        | 0.10     | 0.04       | 0.01     | 0.06    | 0.05     | 1.21       | 0.28     | 9.81    | 1.51     |
| 0.01         | 0.01     | 0.02        | 0.01     | 0.01       | 0.00     | 0.014   | 0.011    | 0.22       | 0.09     | 0.37    | 0.11     |
| 0.53         | 0.13     | 0.41        | 0.10     | 0.04       | 0.02     | 0.03    | 0.034    | 21.86      | 0.94     | 15.41   | 0.97     |
| 0.04         | 0.01     | 0.04        | 0.01     | 0.01       | 0.00     | 0.03    | 0.049    | 29.01      | 0.61     | 27.04   | 0.48     |
| 0.91         | 0.32     | 1.39        | 0.33     | 0.04       | 0.03     | 0.128   | 0.086    | -          | -        | -       | -        |
| 9.31         | 0.36     | 8.70        | 0.36     | 0.16       | 0.08     | 0.051   | 0.13     | -          | -        | -       | -        |
| -            | -        | -           | -        | -          | -        | -       | -        | 47.51      | -        | 44.27   | -        |
| 95.39        | -        | 94.95       | -        | 97.64      | -        | 97.01   | -        | 99.81      | -        | 96.89   | -        |
|              |          |             |          | on 11 O    |          |         |          | on 6 O     |          |         |          |
| 3.14         | 0.06     | 3.07        | 0.06     | 4.02       | 0.04     | 3.94    | 0.04     | -          | -        | -       | -        |
| 0.00         | 0.00     | 0.00        | 0.00     | 0.00       | 0.00     | 0.00    | 0.00     | -          | -        | -       | -        |
| 2.78         | 0.08     | 2.89        | 0.08     | 1.97       | 0.06     | 2.07    | 0.05     | -          | -        | -       | -        |
| 0.00         | 0.00     | 0.00        | 0.00     | 0.00       | 0.00     | 0.00    | 0.00     | -          | -        | -       | -        |
| 0.03         | 0.01     | 0.02        | 0.01     | 0.00       | 0.00     | 0.00    | 0.00     | 0.03       | -        | 0.27    | -        |
| 0.00         | 0.00     | 0.00        | 0.00     | 0.00       | 0.00     | 0.00    | 0.00     | 0.01       | -        | 0.01    | -        |
| 0.05         | 0.03     | 0.04        | 0.03     | 0.00       | 0.00     | 0.00    | 0.00     | 1.00       | -        | 0.76    | -        |
| 0.00         | 0.00     | 0.00        | 0.00     | 0.00       | 0.00     | 0.00    | 0.00     | 0.96       | -        | 0.96    | -        |
| 0.12         | 0.04     | 0.18        | 0.04     | 0.00       | 0.00     | 0.02    | 0.01     | -          | -        | -       | -        |
| 0.78         | 0.03     | 0.73        | 0.03     | 0.01       | 0.01     | 0.00    | 0.00     | -          | -        | -       | -        |
| 6.91         | -        | 6.94        | -        | 6.01       | -        | 6.04    | -        | 2.00       | -        | 2.00    | -        |
| 0.64         | 0.09     | 0.68        | 0.09     | -          | -        | -       | -        | -          | -        | -       | -        |

#### 4.2. Petro- and Microtectonics

In thin section, the metapelite contains a pervasive foliation marked by grain shape preferred orientation of white mica, quartz, pyrophyllite, chloritoid, rutile, and carbonate. This foliation wraps around microlithons of detrital quartz and white mica and chloritoid oriented at high angle to the main foliation (Figures 3g and 5; see next section for the characterization of chloritoid and white mica generations). The stretching lineation is defined by the same mineral assemblage, defining the foliation. S-C-C' structures, asymmetric folds and microlithons with asymmetric strain shadows are visible both at the outcrop and in thin section and are compatible with a top-to-the E sense of shear (Figures 3d, 3g and 5). Locally, rootless isoclinal folds are defined by quartz-rich layers, with a crenulation cleavage parallel to the main foliation (Figures 5a–5e). The white mica-rich layers appear turbid under plane-polarized light due to finely dispersed graphite, rutile, and pyrite, a few microns in size (Figures 5e and 5f). The metaquartzarenite contains numerous detrital monocrystalline or polycrystalline quartz clasts, from a few mm to cm in size and with sharp edges,

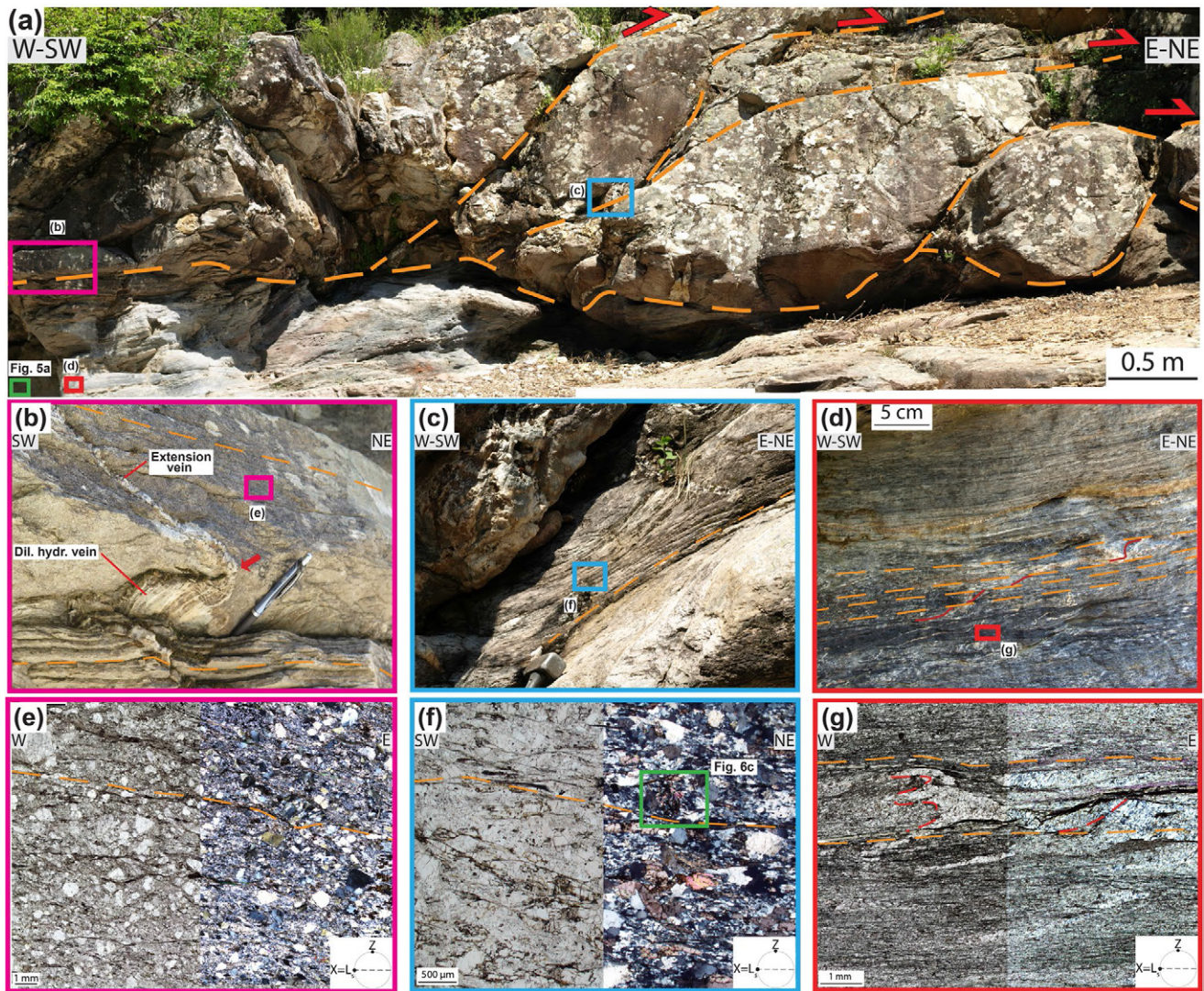


**Figure 3.** Detail of Figure 2. The dashed orange lines highlight some of the mayor horses and the trend of the composite foliation, the arrows the sense of shear. (a) Note the differential erosion of the harder metaquartzarenite and the weaker metapelite. (b) Metaquartzarenite horse (top) displaying a more pervasive foliation at its base in a high-strain zone close to the contact with metapelite (bottom; metapelite is visible in (a)). Extension vein oriented at high angle to the foliation in the horse and dilational hydroshear vein parallel to the foliation at the contact with the metarenite high-strain zone. The red arrow indicates the conjunction between extension and dilational hydroshear veins. Note the quartz fibers marking the stretching lineation oriented parallel to the pen. (c) Details of high-strain zone in metarenite between two horses. (d) Shear zone deforming metapelite at the base of the duplex. The red dashed lines indicate transposed quartz-rich layers. Overall top-to-the E-NE-sense of shear. (e–g) Thin section photos; plane (left) and crossed-polarized light. Thin sections were cut parallel to the stretching lineation ( $X = L_s$ ) and perpendicular to the foliation ( $Z$  parallel to the pole of the foliation). (e and f) Metarenite containing clastic quartz grains with angular edges and a foliation marked by phyllosilicates (orange dashed lines). (g) Metapelite with rootless fold hinges and transposed quartz-rich layers (red dashed lines) wrapped by a phyllosilicate-rich foliation (orange dashed lines).

characterized by undulose extinction and wrapped by the main foliation (Figures 3e, 3f, 6a, and 6b). The foliation is composed of grain shape preferred orientation of white mica, quartz, carpholite, chloritoid, rutile, and carbonate. As in the metapelite, chloritoid is visible both in microlithons oriented at high angle to the foliation or lengthened parallel to it (Figures 6a–6d).

Dilational hydroshears veins are composed of iso-oriented quartz grains, forming up to several cm long fibers interfingered with pale yellow-light green carpholite needles (Figure 4d). Quartz and carpholite fibers define a stretching lineation plunging at low angle to the W-SW and displaying the same orientation as that found in the metapelite and metaquartzarenite (stereonets in Figures 2c and 2d). In thin section,

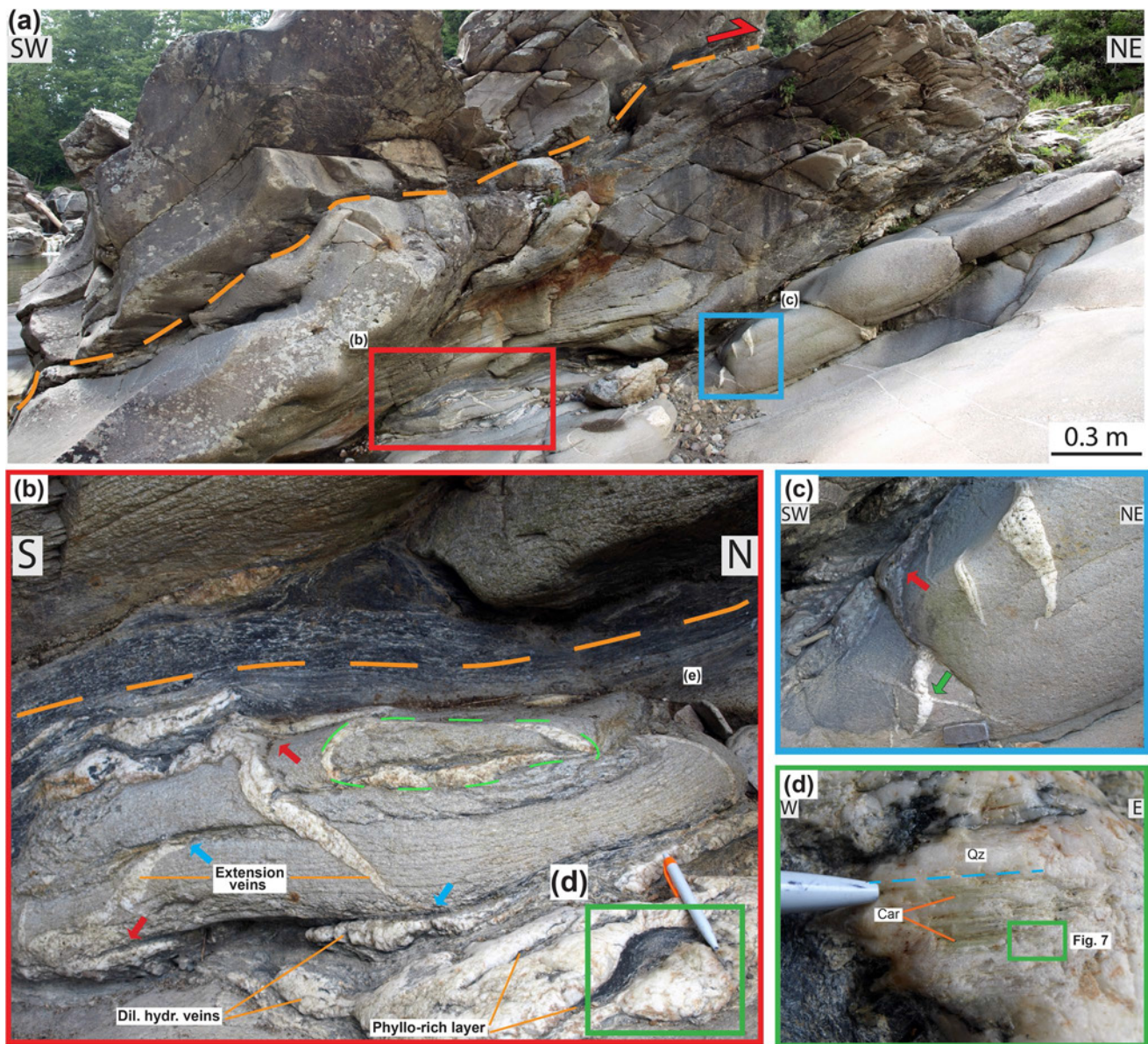


**Figure 4.** (a) Metarenite bands and veins. (b) Detail of dilational hydroshear and extensional veins occurring in metapelite (bluish color) and metaquartzarenite (gray). The red arrows indicate the conjunction between dilational hydroshear and extension veins, the blue arrows the termination of extension veins. A few veins are deformed by noncylindrical folds (green dashed line). The dashed orange line indicates the foliation trace in metapelite. The pen is oriented subparallel to the stretching lineation. Phyllosilicate-rich layers included in dilational hydroshear veins are shown. (c) Extension veins in metaquartzarenite cut by younger quartz veins (green arrow). (d) Dilational hydroshear vein seen in a section parallel to the foliation with quartz and carpholite (greenish-yellowish) fibers oriented E-W (dashed blue line), parallel to the stretching lineation of the host-rock. Mineral abbreviations of this and following figures are from Whitney and Evans (2010).

quartz fibers appear as single-grain crystals with a length from several millimeters to centimeters, high aspect ratios (up to 1:15), undulose extinction, and incipient grain size reduction along grain boundaries (Figures 7b–7d). K-rich mica and pyrophyllite-rich layers occur as inclusions within the veins; they have a thickness of a few mm and are oriented parallel to the lengthening of the fibers (Figures 7a, 7b, 8a, and 8b). These layers appear murky due to graphite, rutile and pyrite inclusions, a few microns in size, and locally form rootless folds. Several fluid inclusion bands are present oriented at high angle to the lengthening of the fibers, with a spacing between bands of a few tens of microns and containing liquid + vapor phases (Figures 7c, 7d and 8c–8f). Carbonate occurs along layers parallel to the fibers and along fractures cutting through them.

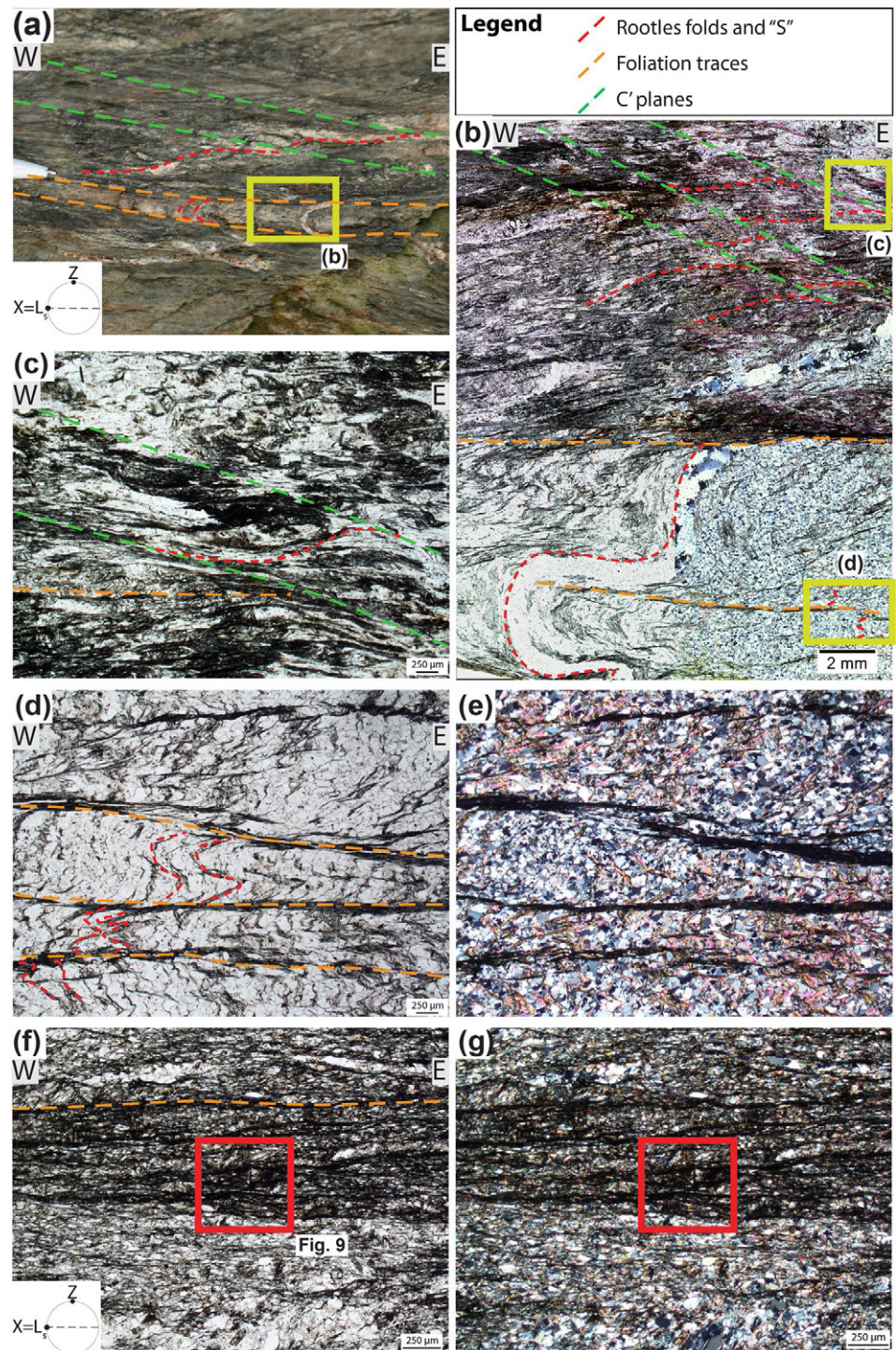


**Figure 5.** (a and b) Outcrop and thin-section photos of metapelite. The dark bands are composed of graphite and phyllosilicates, the bright bands of quartz. Locally, rootles fold hinges are preserved in microlithons and display a pervasive crenulation cleavage (see locations in Figure 3a). (c) Detail of S-C-C' structures indicating a top-to-the-E sense of shear. (d and e) Detail of rootless fold hinges and crenulation cleavage. (f, g) Phyllosilicate-rich layer with a pervasive subhorizontal foliation wrapping around chloritoid (see locations in Figure 3d; detail of site in Figure 9). (b): plane (left) and crossed-polarized light; (c, d, f): plane-polarized light; (e, g): crossed-polarized light.

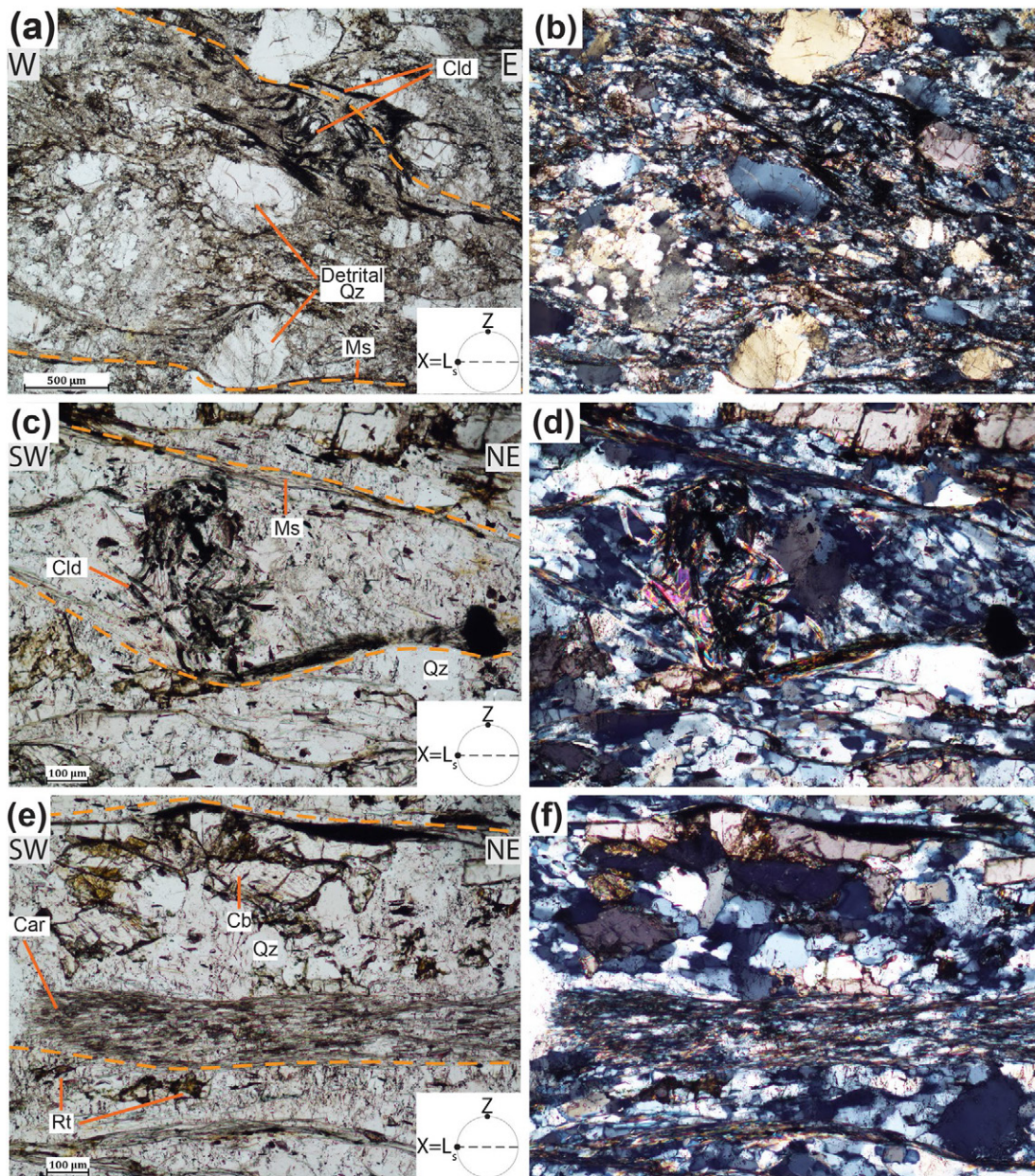


**Figure 6.** Metarenite thin section photos. (a and b) Low-strain horse displaying angular quartz detrital grains and chloritoid growing at high angle and parallel to the main foliation (see locations in Figure 3b). (c–f) High-strain zone between two horses with chloritoid in microlithon wrapped by the main foliation composed of white mica, chloritoid, carpholite, and rutile (see locations in Figure 3c). Plane (left) and crossed-polarized light. The dashed orange lines indicate the foliation traces.

Inclusion bands oriented perpendicular to the lengthening of the quartz fibers are invariably interpreted as resulting from incremental crack-seal growth increments during progressive fracturing and veining, with repeated fracturing and sealing of the vein by mineral precipitation (sketch and cartoon in Figures 7e and 7f, Cox & Etheridge, 1983; Fagereng et al., 2011; Koehn & Passchier, 2000; Trepmann & Seybold, 2019; Ujiie et al., 2018). Additionally, included phyllosilicate-rich layers of variable thickness separating quartz and carpholite fibers allow for the opening of the dilational hydroshear veins at high angle to the foliation, exploiting weak foliation planes of the host-rock (called microtransforms, inclusion trails, and phyllosilicate inclusion bands in Fagereng et al., 2011; Koehn & Passchier, 2000; Ujiie et al., 2018, respectively; see Section 5.3 for discussion).

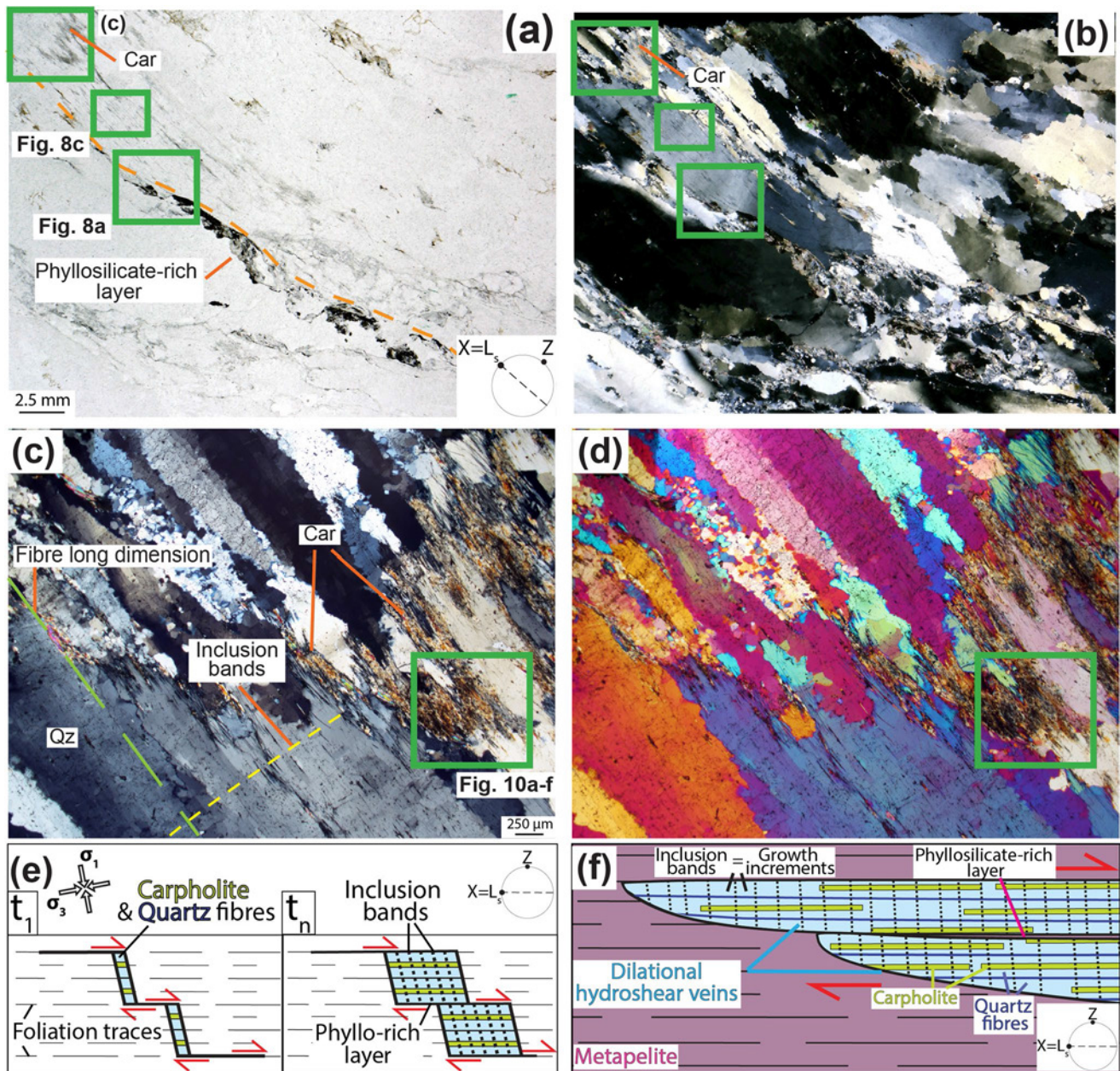


**Figure 7.** Microphotographs of dilational hydroshear veins. (a and b) Thin-section scan with iso-oriented centimetric quartz fibers exhibiting undulose extinction, and acicular carpholite (location of thin section in Figure 4d). The dashed orange line indicates the trend of the phyllosilicate-rich layer, parallel to the host-rock foliation. Plane and crossed-polarized light, respectively. (c and d) Detail of interfingered quartz and carpholite. Note that the quartz fibers are monocrystalline, with incipient grain size reduction preferentially at the edges. Crossed-polarized light and crossed-polarized light with gypsum plate inserted. (e and f) Sketch and cartoon illustrating the progressive formation of dilational hydroshear veins. (e) Inclusion bands mark growth increments oriented perpendicular to the long dimension of the crystals and vein boundaries; the orientation of the greatest and least compressive stresses  $\sigma_1$  and  $\sigma_3$  is shown,  $t_1$  = time at stage 1,  $t_n$  = time after n stages (based on Fagereng et al., 2010; Koehn & Passchier, 2000). (f) Note the phyllosilicate-rich layer between the two dilational hydroshear veins, suggesting that the opening of the dilational hydroshear veins occurred along the weak foliation planes.

### 4.3. X-Ray Compositional Mapping and Mineral Chemistry

One X-ray compositional map was obtained from a metapelite sample and two from quartz and carpholite dilational hydroshear veins (mineral abundances and sample locations are shown in Tables S2 and S3). In detail, the maps in the dilational hydroshear veins were acquired on a carpholite and pyrophyllite-rich layer and on a phyllosilicate-rich layer. In the metapelite, chloritoid displays the same compo-

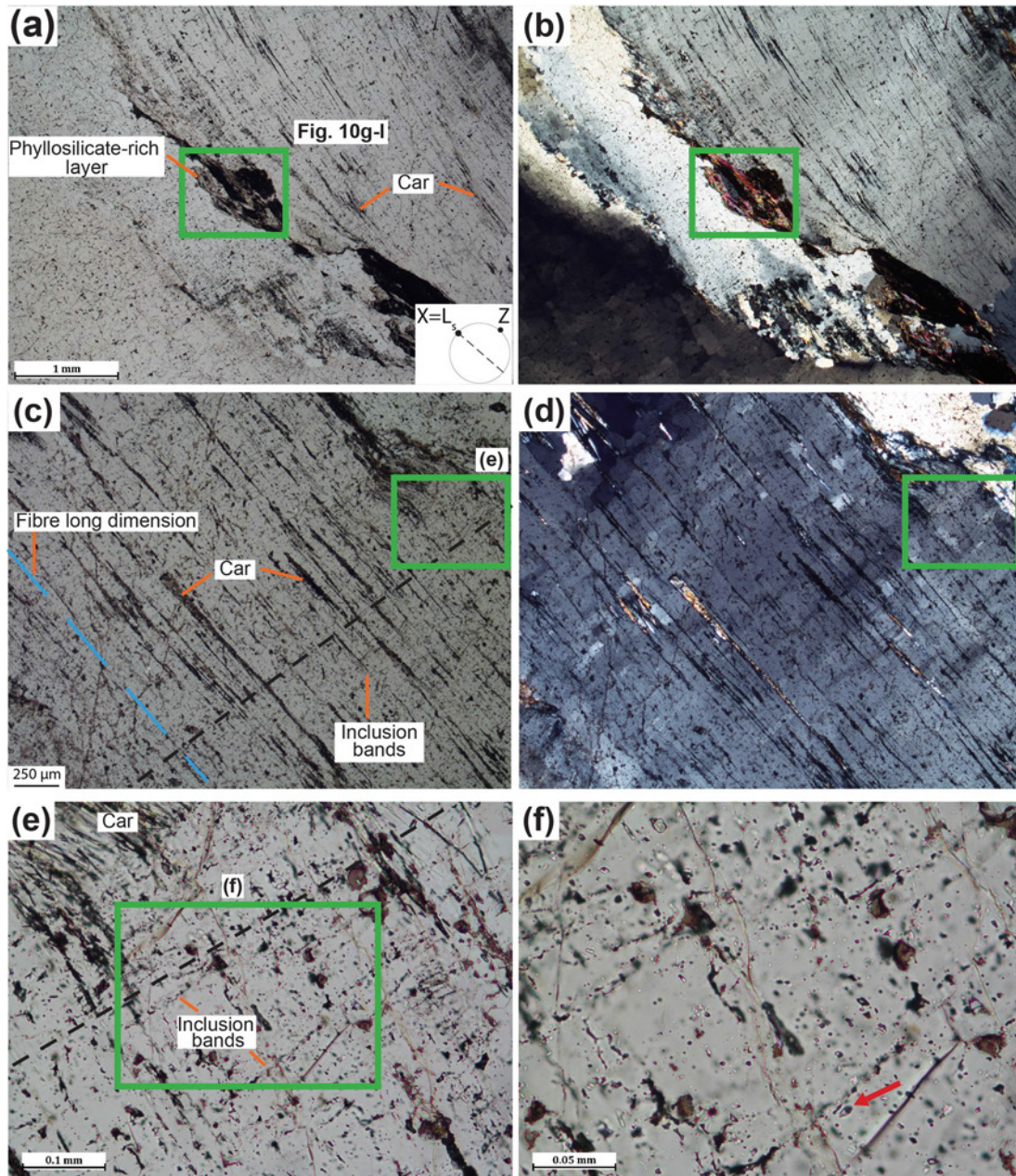


**Figure 8.** Thin section photos of quartz and carpholite dilational hydroshear veins (see locations in Figure 4d). (a and b) Phyllosilicate-rich layer, appearing turbid due to micrometer-sized graphite and rutile inclusions, and quartz and carpholite-rich layers. Quartz fibers display undulose extinction and grain size reduction at their edges. (c and d) Iso-oriented carpholite needles in quartz grain (blue dashed line). The black dashed line indicates the orientation of inclusion bands. (e and f) Inclusion bands perpendicular to the lengthening of the fibers, few tens of microns apart. The inclusions are composed of fluid and gas phases (arrow). Plane (left) and crossed-polarized light.

sition both in crystals arranged perpendicularly to the main foliation and in those parallel to it, with a  $X_{Mg}$  content comprised between 0.16 and 0.25 (Figure 9 and Table 1). In both metapelite and dilational hydroshear vein, muscovite grains are phengitic and generally characterized by a higher Si content in the core (3.2–3.3;  $X_{Mg}$  0.6–0.7; Figures 9e, 9f, 10k, and 10l) and lower Si content around the cores and along grain boundaries (3–3.2;  $X_{Mg}$  0.5–0.7), although more complex zoning locally also occurs (see discussion Section 5.1).

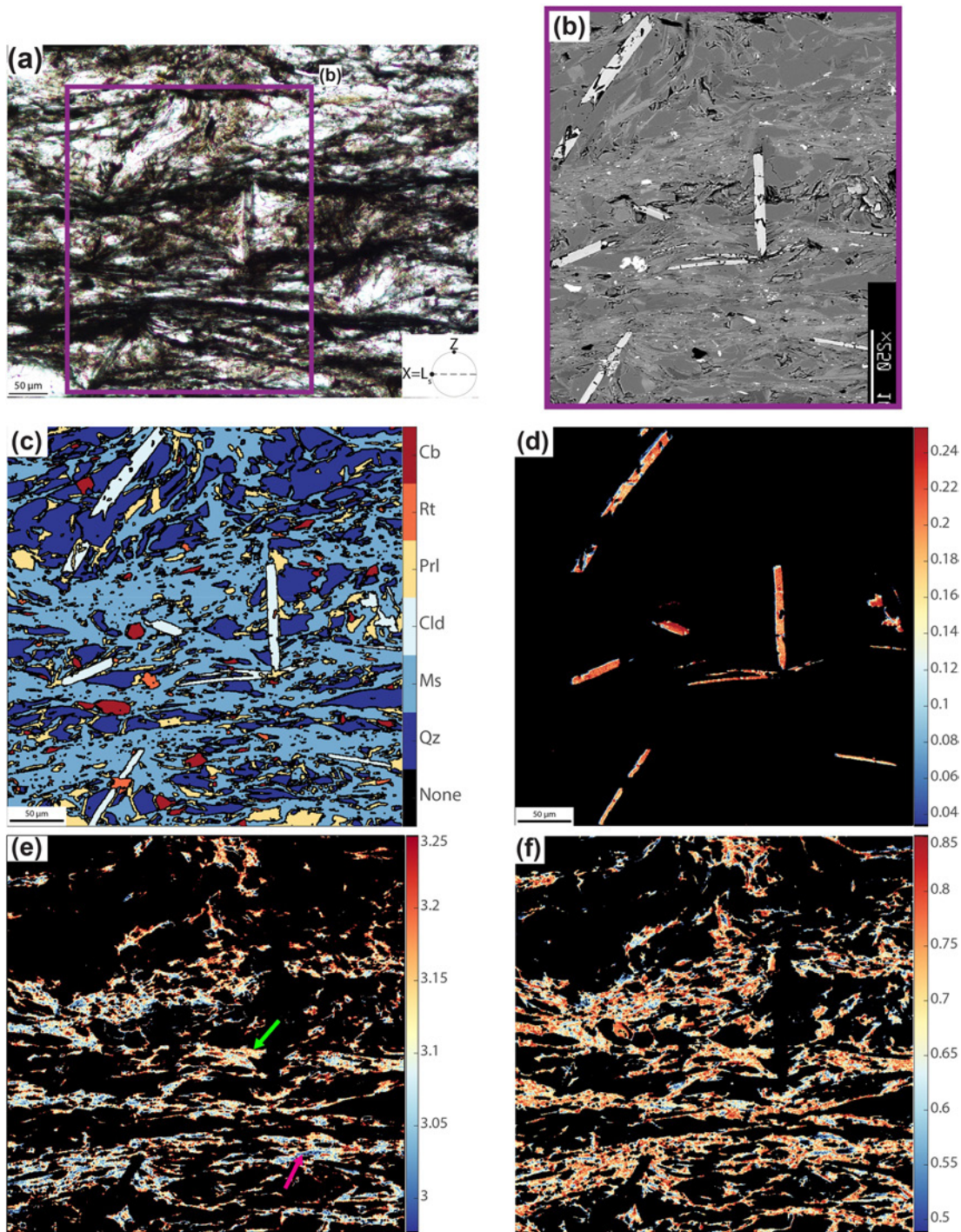


**Figure 9.** Detail and compositional maps of metapelite with phyllosilicate-rich layer wrapping around chloritoid microliths (see locations in Figures 3d and 5f). (a and b) Optical plane-polarized light photo and backscattered electron images (BSE) image displaying chloritoid grains parallel and at high angle compared to the foliation. (c–f) Compositional X-ray maps. (c) Mineral phases. (d) Chloritoid displays similar  $X_{Mg}$  content in all the different microstructural sites. (e and f) Si apfu and  $X_{Mg}$  content, respectively, of muscovite; high and low Si contents shown by the green and purple arrows, respectively.

In the dilational hydroshear vein, carpholite exhibits a subtle chemical variation in the  $X_{Mg}$  content, with values up to 0.7 in the core and 0.6 in the rims (Figure 10f). Carpholite is intergrown with quartz and pyrophyllite. Noteworthy, most carpholite grains in contact with pyrophyllite have lobate edges and peninsular features and some larger pyrophyllite grains are oriented at high angle to the fibers and foliation

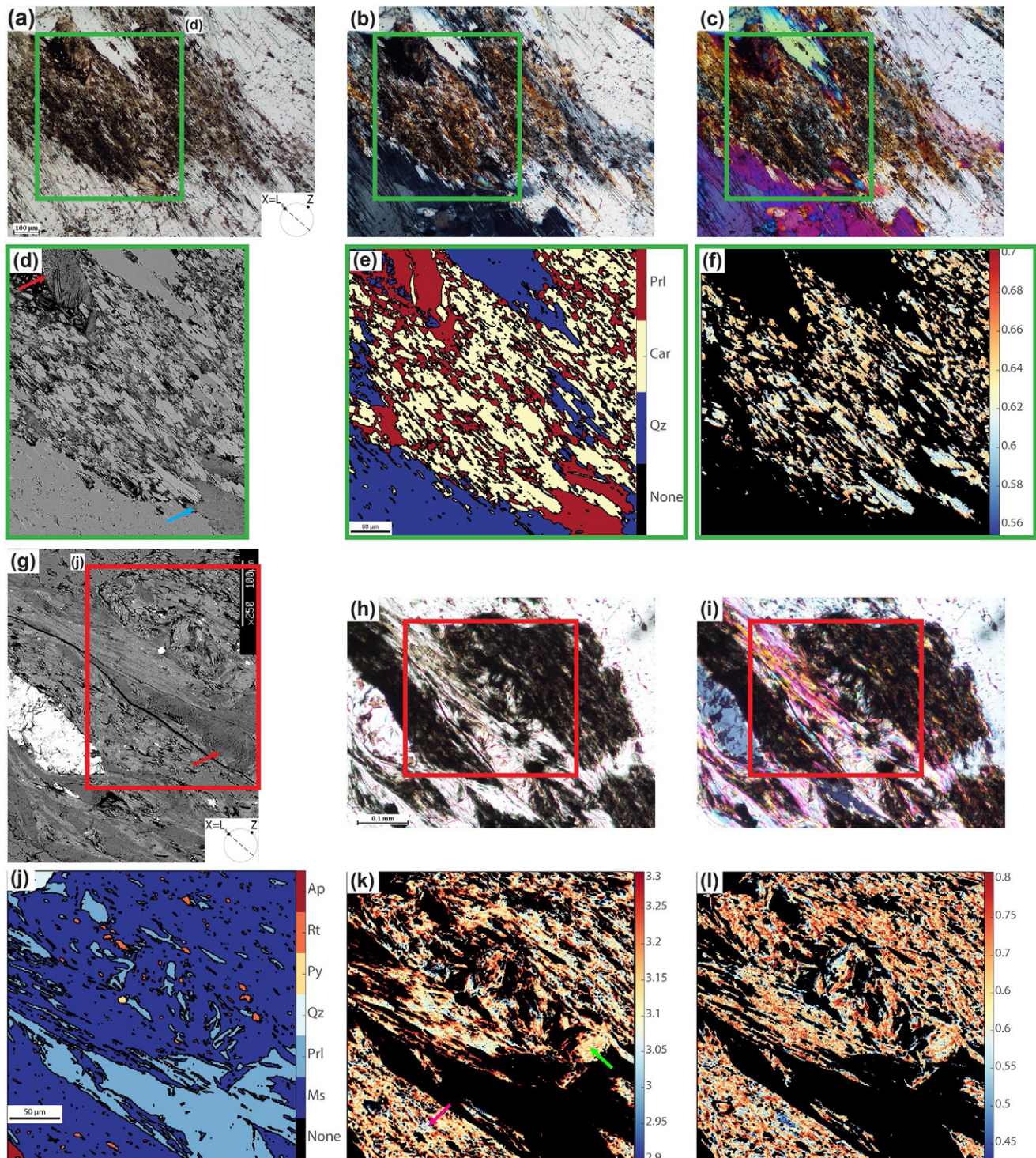


**Figure 10.** Detail and compositional maps of the quartz and carpholite dilational hydroshear vein: (a–f) quartz and carpholite-rich layer, (g–l) phyllosilicate-rich layer. (a, d) Quartz and carpholite are interfingered; pyrophyllite overgrows carpholite at grain boundaries (light blue arrow in (d)) and at high angle to the fibers (red arrow in (d)). Optical plane-polarized light, crossed-polarized light, crossed-polarized light with gypsum plate inserted and BSE image, respectively. (e and f) Compositional X-ray maps. (e) Mineral phases. (f) Carpholite shows cores higher in  $X_{Mg}$  content than rims (see locations in Figures 4d and 7a). (g–i) Backscattered electron images (BSE) image and plane and crossed-polarized light thin-section photos displaying muscovite appearing turbid due to micrometer-sized inclusions of graphite, rutile and pyrite and limpid pyrophyllite. Note the pyrophyllite growing at high angle compared to the foliation (red arrow in (g)). (j–l) Compositional X-ray maps. (j) Mineral phases. (k and l) Si apfu and  $X_{Mg}$  content, respectively, of muscovite; high and low Si contents shown by the green and purple arrows, respectively.

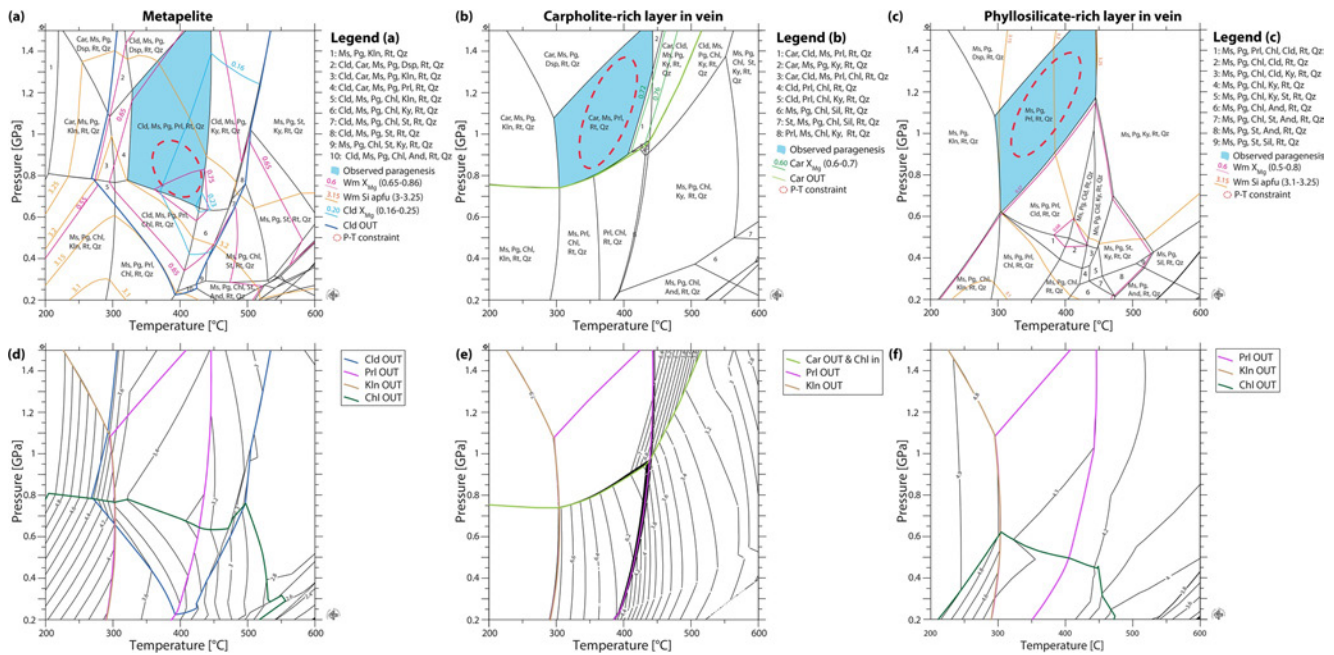


**Figure 11.** Equilibrium phase diagrams and thermodynamic modeling of H<sub>2</sub>O content in solids (wt%), with mineral-out reactions highlighted (see legend). (a, d) Metapelite. (b, e) Carpholite-rich layer in the dilational hydroshear vein. (c, f) Phyllosilicate-rich layer in the dilational hydroshear vein.

(light blue and red arrows, respectively, in Figures 10d and 10g; see Section 5.1 for interpretation). In the metapelite, carbonate grains have a dolomite core and an ankerite rim.

#### 4.4. Geothermobarometry

Local bulk compositions were extracted from the three compositional X-ray maps and used to compute isochemical phase diagrams (Table S2; see methods). In the metapelite, the predicted assemblage matches the observed paragenesis in the light-blue field of Figure 11a, with a minor discrepancy of 5 vol% lower pyrophyllite in the predicted assemblage than the observed assemblage (Table S2). The measured phengitic muscovite Si and X<sub>Mg</sub> isopleths and the chloritoid X<sub>Mg</sub> isopleths intersect within the light-blue field. Additionally, chlorite was not observed in the sample, constraining the minimum P to values higher than ~0.7 GPa. Therefore, P-T conditions of the metamorphic stage recorded in the metapelite are between 0.7–1 GPa and 350°C–400°C, which fit the observed paragenesis and the computed isopleths (red dashed ellipsis in Figure 11).

In the quartz and carpholite, dilational hydroshear vein two isochemical phase diagrams were computed: one for the carpholite and pyrophyllite-rich layer and one for the muscovite and pyrophyllite-rich layer (Figures 11b and 11c, respectively). In the first diagram, the predicted assemblage conforms with the observed paragenesis in the light-blue field, with a discrepancy of 10 vol% higher carpholite and 7 vol% lower pyrophyllite content in the predicted assemblage than the observed assemblage (Table S2; see discussion Section 5.1). The minimum value of predicted carpholite X<sub>Mg</sub> is 0.72, which is 0.02 higher than the maximum measured value. In the phyllosilicate-rich layer, the total amount of the phyllosilicates in the predicted and observed assemblages (muscovite + paragonite + pyrophyllite) is similar, although pyrophyllite is modeled ~10 vol% lower than the observed value. Muscovite Si and X<sub>Mg</sub> isopleths intersect in the field of the observed paragenesis. In summary, the inferred P-T conditions for the development of the dilational hydroshear vein are ~1.1 GPa and 350°C.

In both the metapelite and the dilational hydroshear vein, muscovite rims, and grain boundaries characterized by lower Si apfu contents would indicate lower P-T conditions (orange isopleths in Figures 11a and 11c; see discussion Section 5.1).

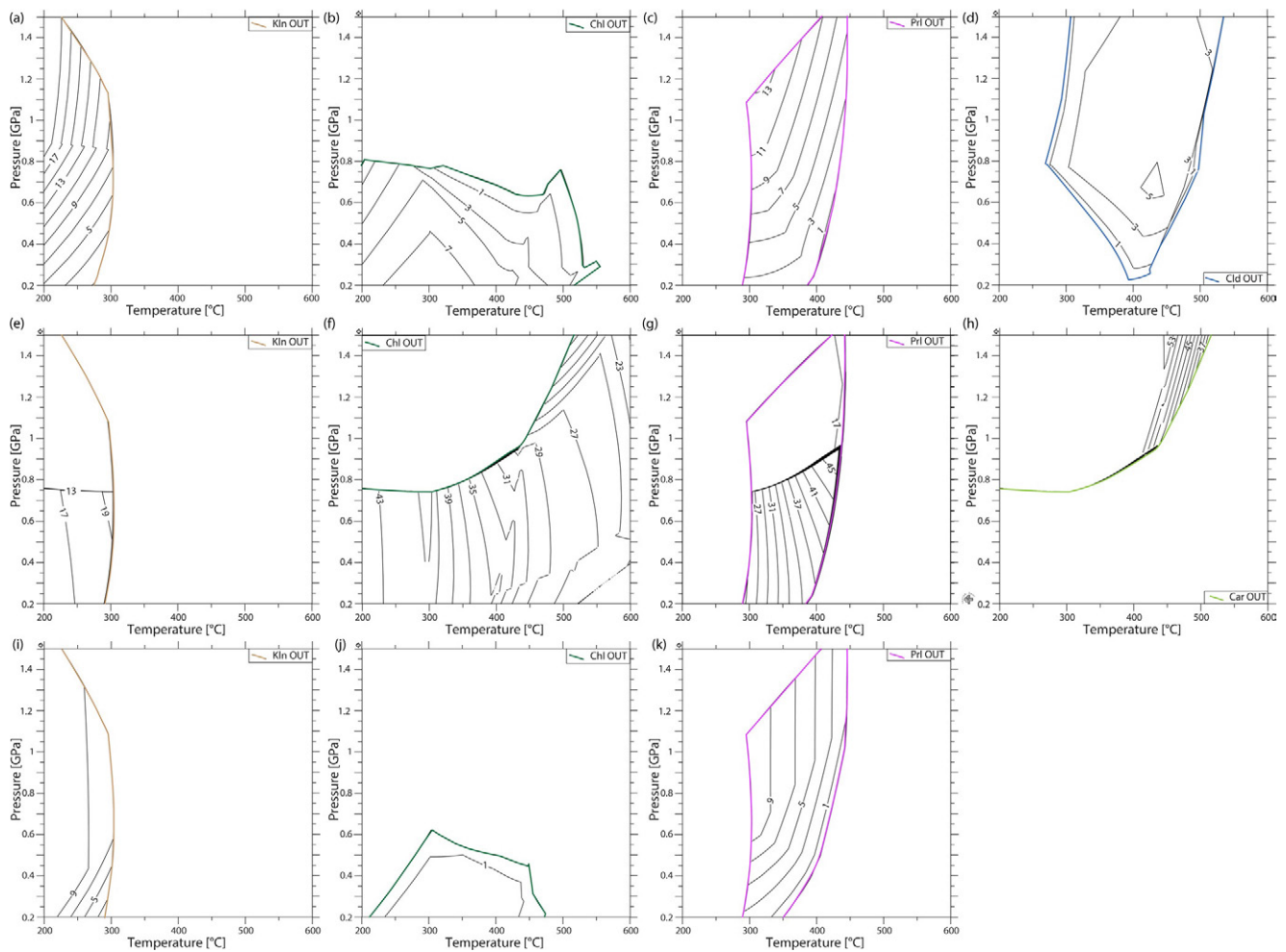


**Figure 12.** Modal amount of kaolinite, chlorite, pyrophyllite, carpholite, and chloritoid (vol%). (a–d) Metapelite. (e–h) Carpholite-rich layer in dilational hydroshear vein. (i–k) Phyllosilicate-rich layer in dilational hydroshear vein.

#### 4.5. Dehydration Along the Prograde P-T Path of the NA

Diagrams of the  $H_2O$  content in solids (wt%; Figures 11d–11f) highlight how  $H_2O$  content drops in correspondence of specific mineral destabilization reactions. This is also visible from Figure 12, where modal amounts of mineral phases (vol%) and  $H_2O$  content of the mineral phases (wt%) are shown for a prograde P-T path characteristic for the Northern Apennines (from 0.5 GPa and 200°C to 2 GPa and 575°C, based on data from this study and Bianco et al., 2019, Figures 12 and 13 and Table S4). In detail, kaolinite destabilization produces a decrease of ~0.9 wt% of the total  $H_2O$  content in the mineral phases in metapelite (from 4.6 to 3.5 wt%), 0.7 wt% in the carpholite-rich layer and 0.6 wt% in the phyllosilicate-rich layer of the dilational hydroshear vein between 0.5 GPa–200°C and 1 GPa–325°C (Figures 11d–11f and 13). Pyrophyllite-out produces a decrease of 0.4 wt% in metapelite, 0.8 wt% in carpholite-rich layer of the dilational hydroshear vein, and no variation in the phyllosilicate-rich layer of the dilational hydroshear vein between 1 GPa–325°C and 1.5 GPa–450°C. Carpholite destabilization is responsible for a progressive decrease of 3.3 wt% between 1.5 GPa–450°C and 2 GPa–575°C in the carpholite-rich layer of the dilational hydroshear vein, despite contemporaneous chloritoid formation. In both metapelite and dilational hydroshear vein, chlorite destabilization does not coincide with an appreciable decrease in  $H_2O$  content. This is seen well in the carpholite-rich layer of the dilational hydroshear vein, where chlorite decreases from 42 to 0 vol% and carpholite increases from 0 to 51 vol% between 0.7 GPa–250°C and 0.8 GPa–275°C (Figures 12f and 12h).

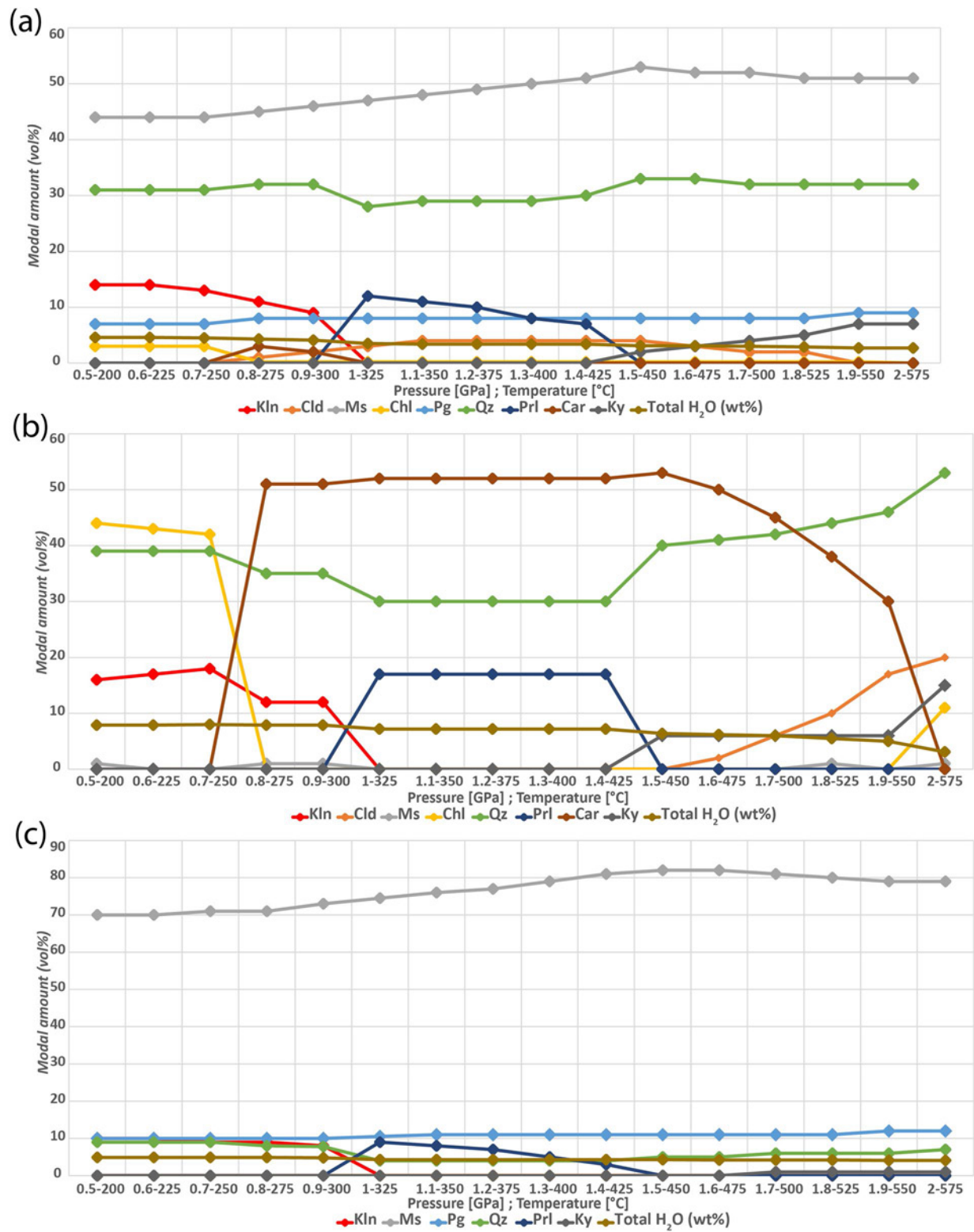


**Figure 13.** Plot of the vol% of the hydrous mineral phases and wt% of H<sub>2</sub>O in solids (Total H<sub>2</sub>O) along the prograde P-T path of the Northern Apennines from 0.5 GPa and 200°C to 1.9 GPa and 550°C (based on P-T data from this study and from Bianco et al., 2019). (a) Metapelite. (b) Carpholite-rich layer in dilational hydroshear vein. (c) Phyllosilicate-rich layer in dilational hydroshear vein. See Table S4 for further details.

Summarizing, kaolinite, pyrophyllite, and carpholite destabilization reactions are the main releasers of aqueous fluid in the studied rocks (see discussion Section 5.3).

## 5. Discussion

### 5.1. P-T Conditions of HP Contractional Duplex Formation, Top-to-E Shearing and Geodynamic Implications for the HP Evolution of the NA

Our new field and microstructural data suggest that the described metamorphic foliation and extensional and dilational hydroshear veins exhibit mutually overprinting relationships (veins are from parallel to high angle to the foliation but are locally also deformed and transposed by ductile shear zones; Section 4.1) and thus are broadly coeval. Additionally, geometric and kinematic considerations indicate that they formed in response to the same stress field and that they constrain the same regional kinematic framework. Thermodynamic modeling constrains the development of the foliation in the metapelite to between 0.7–1 GPa and 350°C–400°C (Figure 11; Section 4.4). Quartz and carpholite dilational hydroshear veins formed at ~1.1 GPa and 350°C. These P-T estimates thus agree with our interpretation of a common structural origin, although the veins formed at slightly higher *P* and lower *T* conditions. The slightly lower P-T conditions estimated for the foliation may also indicate that the latter was partially re-equilibrated at the beginning of the retrograde path, thus during exhumation. This notwithstanding, the documented difference in *P* and *T* is well within the range of uncertainty of thermodynamic modeling ( $\pm 0.2$  GPa and 50°C).

In both the metapelite and dilational hydroshear veins, the X-ray compositional mapping of muscovite highlights complex zoning, with a generally lower Si content along rims and grain boundaries (Figures 9e and 10k, Section 4.3). This probably reflects the partial reequilibration and replacement of higher Si content muscovite during retrogression, as described by Airaghi et al. (2017) and Giuntoli, Lanari, et al. (2018). We thus interpret muscovite with lower Si contents to mark the incipient retrogression of the system, in agreement with the thermodynamic modeling results (orange isopleths in Figures 11a–11c, Section 4.4). Additionally, partial retrogression is also evidenced by pyrophyllite overgrowing carpholite grains in dilational hydroshear veins, indicative of replacement processes occurring at lower pressure (Figures 10 and 11b, 11c; e.g., Giuntoli, Menegon, et al., 2018; Putnis & Putnis, 2007). Finally, retrogression is also supported by thermodynamic modeling that predicts higher carpholite and lower pyrophyllite contents (vol%) in dilational hydroshear veins compared to the observed values.

In the metapelite, the two observed generations of chloritoid, oriented at high angle and parallel to the foliation, respectively, are characterized by the same chemistry, thus suggesting that they formed at similar P-T conditions (Figures 9a–9d and light-blue isopleths in Figure 11a). A possible scenario for this contemplates a static growth for the first generation, followed by the development of the foliation and the second and synkinematic chloritoid generation, with partial reorientation of the first generation and its preservation in microlithons. Another possibility, however, is that the first generation of chloritoid also grew parallel to the foliation but was successively reoriented by a process of crenulation during which an axial plane foliation and the second syn-kinematic generation were formed. Although locally we do observe a crenulation cleavage (Figure 5 and Section 4.2), we never observed the first generation of chloritoid in microlithons marking fold hinges or oriented subparallel to the crenulation axial planes, and thus prefer the first scenario. Similar microstructural observation on chloritoid zoned in  $X_{Mg}$  are reported in the Apuane metamorphic units, where chloritoid formed during consecutive deformation stages (Molli et al., 2002 and references therein).

In summary, field observations integrated by thermodynamic modeling allow us to conclude that mylonitic foliation and dilational hydroshear veins both formed during the same top-to-the E-NE thrusting phase under blueschists facies conditions between 0.7–1.1 GPa and 350°C–400°C. Partial retrogression of both foliation and dilational hydroshear veins is suggested by the lower Si content of muscovite grain boundaries and pyrophyllite locally overgrowing carpholite, pointing to incipient exhumation recorded by the studied structures.

Our new P-T estimates confirm that also the Palaeozoic basement of the Tuscan Metamorphic Units was subducted to a depth corresponding to P-T conditions comparable to those experienced by the early Triassic Verrucano Formation metasediments, as described for the Monti Pisani, where the Paleozoic basement

has been shown to have been metamorphosed at 0.9–1 GPa and 470°C during the Apennine orogeny (Lo Pò & Braga, 2014). Comparable P-T conditions are described for the Verrucano Formation metasediments of the Monte Quoiio-Montagnola Senese subunit and the Monte Leoni-Farma subunit of nearby sectors of the MRU, with  $P \geq 1.1$  GPa and  $T$  370–420°C and 0.8–1 GPa and 400°C–420°C, respectively (Brogi & Giorgetti, 2012; Giorgetti et al., 1998). Similar P-T conditions are also described for the Verrucano Formation metasediments of the Monte Argentario, with peak metamorphic conditions of  $>0.8$  GPa and 300°C–400°C, retrograde conditions of  $<0.5$  GPa and 350°C and a final stage below 300°C (Theye et al., 1997). Noteworthy, at Monte Argentario the mineral phases related to peak P-T conditions are only preserved in microlithons, while the main fabric visible in the field is related to retrograde greenschist facies conditions, confirming that HP fabrics are generally scanty and poorly preserved in the NA.

In the Apuane metamorphic units, similar P-T conditions are reported for the more internal Massa Unit, which records higher P-T (0.6–0.8 GPa and 420°C–500°C) than the more external Apuane Unit (0.4–0.6 GPa and 350°C–450°C; Franceschelli et al., 1986, 1997; Jolivet et al., 1998; Molli et al., 2000, 2002). A thrust is believed to have superposed the Massa unit onto the Apuane unit during retrograde HP conditions, in the stability field of chloritoid-pyrophyllite. This tectonometamorphic event possibly marked a stage of syn-collisional exhumation in the Apuane metamorphic units (Molli et al., 2000). Ryan et al. (2021) propose syn-collisional exhumation in the forming orogenic wedge within the Apenninic subduction channel based on kinematic evidence from the Eastern Elba Nappe Stack that accounts for upward extrusion of the Acquadolce Subunit, a high-strain lithotectonic unit of the Tuscan Metamorphic Units, containing the Elba Island HP assemblages (Bianco et al., 2015, 2019; Papeschi et al., 2020), by coeval normal shearing and thrusting at its top and base, respectively. Based on similar P-T conditions, we speculate that the HP contractional fabrics of the Massa Unit and the MRU may represent the deepest tectonometamorphic structures preserved in the NA, recording the onset of synorogenic exhumation within the subduction channel, although absolute dating of these structures would be needed to confirm that they are cogenetic. Similarities between these two geological units were already suggested by Burgassi et al. (1979) and Rau and Tongiorgi (1974), supporting the idea that these units represent the northern- and southernmost exposed portions of the same HP terrane.

Another scenario was proposed in literature for the exhumation of HP metamorphic units in the NA. According to it, the formation of HP units was closely followed by syn-orogenic exhumation by deeply reaching top-to-the E low-angle normal faulting (detachment faults). During exhumation, pervasive greenschist facies re-equilibration of the HP fabrics occurred, and continuous underthrusting of cold Adriatic units maintained cold gradients in the subduction zone (e.g., Carmignani et al., 1994; Jolivet et al., 1998; Rossetti et al., 1999). Evidence of low-angle normal faulting is described from Gorgona and Giglio islands (Tuscan Archipelago). At Gorgona Island, metasediments belonging to a lower tectonometamorphic units record 1.5 GPa and 350°C and locally preserve a HP stretching lineation defined by carpholite and quartz oriented N-S. An upper tectonic unit composed of metabasic rocks and serpentinites experienced 0.6–0.8 GPa and  $>300$ °C. The contact between the two units is marked by a greenschist facies, top-to-the E/SE ductile shear zone interpreted as an extensional detachment (Jolivet et al., 1998; Rossetti et al., 2001). At Giglio Island, the same authors ascribe the main fabrics of the Verrucano Formation metasediments to greenschist facies conditions, with HP relics only preserved in microlithons, and interpret those fabrics to reflect a top-to-the E/SE detachment (Jolivet et al., 1998; Rossetti et al., 1999).

We speculate that out-of-sequence thrusting or syn-orogenic extrusion of tectonic units preserving top-to-the E contractional structures at their base and W-verging extensional structures at their top can be held responsible for the exhumation of HP metamorphic units to shallower crustal levels, as also proposed by Brogi and Giorgetti (2012), Molli, Carlini, et al. (2018), Molli et al. (2000), Montomoli et al. (2009), Storti (1995) for the Tuscan Metamorphic Units and Keller and Piali (1990), Papeschi et al. (2020), Pertusati et al. (1993), and Ryan et al. (2021) for the Elba Island. However, future geochronological work is needed to test that the compared structures are coeval. Finally, exhumation to shallower structural levels and up to the surface was possible by both high- and low-angle normal faulting (Molli, Carlini, et al., 2018). We propose that subduction of continental units to the blueschist facies conditions documented for the NA can be favored by the limited thickness of these units (maximum of a few km, e.g., Azzaro

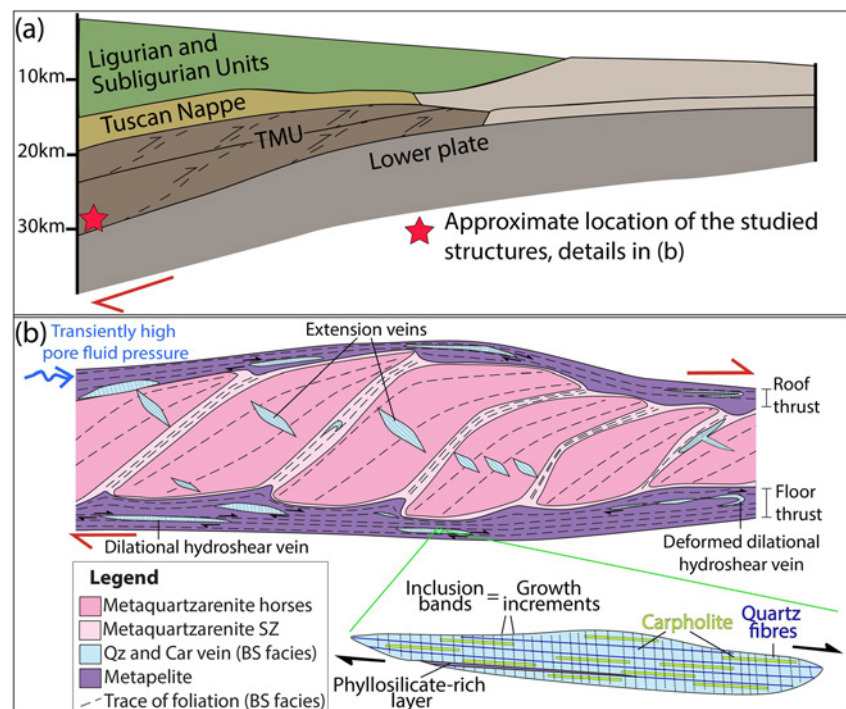


**Figure 14.** (a) Tectonic sketch of the Apenninic wedge during subduction of the Tuscan Metamorphic Units (TMU; Modified after Molli, Brovarone, et al., 2018). (b) Summary sketch of the studied duplex. Dehydration reactions triggered transiently high pore pressure responsible for dilational hydroshear veins formation.

et al., 1976) before stacking, as recently proposed for continental units of the Sesia Zone in the Western Alps (Engi et al., 2018; Giuntoli & Engi, 2016; Giuntoli, Lanari, et al., 2018).

## 5.2. Quartz and Carpholite Veins in the Apennines

Brogi and Giorgetti (2012) reported quartz and carpholite veins from the Verrucano Formation metasediments of the Monte Quoiio-Montagnola Senese subunit of the MRU (see geological setting for further details). They described two mutually overprinting generations of tension gashes arranged in en-échelon arrays and interpreted them as due to fracturing and veining during bulk progressive rotation within a noncoaxial brittle-ductile flow associated with thrusting with the overall Apennine east vergence. In the Arenarie di Poggio al Carpino Formation, we recognized only one generation of carpholite intergrown with quartz fibers in the dilational hydroshear veins. These are oriented parallel to the foliation in the metapelite and metaquartzarenite (Section 4.1). Moreover, carpholite invariably marks the stretching lineation recorded in the host-rock. Some veins are locally intensely folded, with the development of non-cylindrical folds, with geometries compatible with top-to-the E shearing. Therefore, our observations suggest that brittle and ductile deformation alternated at similar metamorphic conditions, mutually overprinting during top-to-the E thrusting (Figure 14).

The dilational hydroshear veins within the metamorphic MRU described in our work are similar to the veins described in the Verrucano Formation metasediments of the Giglio Island, where also similar P-T were found (Capponi et al., 1997; Rossetti et al., 1999). At the meso and microscale, the veins from both the MRU and Giglio Island are characterized by intergrown quartz and carpholite fibers and fluid inclusion bands in quartz fibers (Figure 7 of Rossetti et al., 1999; see Section 5.3). Quartz and carpholite intrafolial veins are also reported from metasediments on Gorgona Island, metamorphosed at 1.5 GPa and 350°C (Jolivet et al., 1998; Rossetti et al., 2001; see section 5.1 for further details). Quartz fibers thereof have abundant bands-forming fluid inclusions containing liquid + vapor phases, similar to what reported from the veins described in this study. Additionally, fibrous quartz and carpholite veins are also present in the Southern

Apennines, in metasediments belonging to the Ligurian Accretionary Complex that experienced P-T conditions of 1.2–1.4 GPa and 350 °C (Frido Unit, Calabria; Vitale et al., 2013).

### 5.3. Carpholite Dilational Hydroshear Veins, Metamorphic Dehydration Reactions and Deep Episodic Tremor and Slow Slip (ETS) Events

The MRU blueschist facies dilational hydroshear veins share a number of close similarities with dilational hydroshear veins reported from sub-greenschist facies conditions typical of shallow accretionary prisms (Fagereng et al., 2011; Ujiie et al., 2018). In particular, the inclusion bands perpendicular to the lengthening of the fibers, which point to a crack-seal mechanism, and included layers of the host-rock, which represent weak planes exploited for the opening of the veins (Sections 4.1 and 4.2 and sketches in Figures 7e, 7f and 14b).

Dilational hydroshear veins in subducted metasediments are interpreted as a key evidence of fossil ETS, implying the presence of a pore pressure cyclically reaching supra-lithostatic values (Fagereng et al., 2011). The investigated continental HP metasedimentary unit was affected by several dehydration reactions during prograde metamorphism. In these lithotypes, the main carriers and releasers of aqueous fluid are the kaolinite (0.6–0.9 wt%, for the dilational hydroshear vein and metapelite, respectively), pyrophyllite (0.4–0.8 wt%, as above) and carpholite-out reactions (up to ~3.3 wt% for the vein; Section 4.5, Figures 11d–11f and 13). These values constrain the amount of aqueous fluid released from the subducting rocks and not incorporated in newly formed minerals. Evidently, the average supply of aqueous fluid from subducting metasediments depends on the relative proportions of metapelite and quartz and carpholite veins. Importantly, the carpholite-out reaction can produce up to ~0.5–1 wt% aqueous fluid in metasediments rich in carpholite veins. In the MRU, carpholite is <1 vol% of the entire mineral assemblages. Therefore, the contribution of the carpholite-out reaction to the global fluid budget is low, even though it is likely relevant for local mineral reactions, mechanical weakening and deformation in proximity of the veins. Interestingly, in these rocks chlorite destabilization does not result in a decrease in the total H<sub>2</sub>O wt%, because that amount of H<sub>2</sub>O is promptly stored in the forming carpholite. We thus propose that local dehydration reactions triggered transient and cyclic fluid overpressure, reaching and exceeding lithostatic values (e.g. Condit et al., 2020; Muñoz-Montecinos et al., 2020; Peacock, 1990; Saffer & Tobin, 2011). As a result, a temporary shift from ductile to brittle deformation occurred (Figure 14b). Furthermore, part of the fluid released by metamorphic dehydration reactions can be stored in the newly formed veins, allowing aqueous fluid bounded in the crystal structure of neoblastic minerals, such carpholite, to reach greater subduction depths.

Summarizing, based on field and microstructural analysis integrated with thermodynamic modeling and compositional X-ray mapping, we suggest that the described blueschist facies dilational hydroshear veins and mylonitic fabrics represent a geological record of deep ETS and relate to transient cycles of pore pressure variation. Relatively low pore pressure and low strain rates caused diffuse deformation and aseismic creep, whereas high pore pressure and high strain rates embrittled the system producing localized deformation and ETS, as in the model of Bernaudin and Gueydan (2018). In particular, tremor bursts likely generated microfracturing and the formation of dilational hydroshear veins, as also hypothesized by Behr and Bürgmann (2021) and Kirkpatrick et al. (2021). Sealing of fractures rapidly produced a decrease in pore pressure and a new phase of aseismic creep and diffuse deformation at PT conditions dictated by the depth where this cyclic deformation occurred. In dilational hydroshear veins, every incremental crack-seal step, marked by adjacent inclusion bands and spaced a few tens of microns, has been related to repeated tremors, with a recurring time of few years (Ujiie et al., 2018). The maximum length of c. 1 m of dilational hydroshear veins observed in this study is within the range described by Fagereng et al., 2011 (one meter to tens of meters), although in our study area it is difficult to define the lateral extension of the dilational hydroshear veins and estimate the rupture areas due to limited outcrop exposure. Nevertheless, in the MRU similar veins are also reported ~7 km along strike from our study area, where they crop out on an area of ~6 km<sup>2</sup>, as reported by the geological map of Figure 5 of Brogi and Giorgetti (2012; Sections 2 and 5.2). In the Cyclades, Kotowski and Behr (2019) estimated a maximum area of ~0.8 km<sup>2</sup> for the described heterogeneities and hypothesized that that area might represent the source of deep ETS. Therefore, based on the assumption that in the MRU ruptures leading to ETS occur broadly coevally, our estimate of potential source areas would represent the higher spectrum of source area values described for active and fossil subduction zones, as reported in

Figure 15 of Kotowski and Behr (2019) and Figure 11 of Behr and Bürgmann (2021). Future work aimed at describing the deformation mechanisms and estimating the differential stresses and strain rates of the studied structures could further constrain the proposed link with ETS (e.g., Fagereng et al., 2014; Kotowski & Behr, 2019; Molli et al., 2017; Platt et al., 2018)

In subduction settings, deep ETS occur along or close to the subduction interface (e.g., Behr & Bürgmann, 2021; Brown et al., 2009). The Tuscan Metamorphic Units represent continental rocks of the subducting Adriatic lower plate that reached HP conditions before being accreted and exhumed, thus representing the subduction interface, as shown in Section 2 and in the tectonic sketch of Figure 14a and as proposed by several authors (e.g. Carminati & Doglioni, 2012; Molli, 2008; Vignaroli et al., 2009). Additionally, the similarities observed between the quartz and carpholite veins described in this work and the examples distributed along the Apennines would suggest that deep ETS are common phenomena occurring at the scale of the entire orogen (Section 5.2).

#### 5.4. Comparison With Reported Deep ETS in Modern and Ancient Geological Settings

Deep ETS occurring in subduction settings similar to the Northern Apennines are described in modern and seismologically active settings, such as New Zealand, Costa Rica, Alaska and SW Japan, and are interpreted to have occurred in ancient, exhumed geological settings, such as Cyclades (Behr et al., 2018; Kotowski & Behr, 2019), Western Italian Alps (Angiboust et al., 2015; Malatesta et al., 2018), and Alpine Corsica (Molli et al., 2017), Coast Ranges of northern California (Platt et al., 2018) as summarized in Figure 1 of Kirkpatrick et al. (2021) and Figure 3 of Behr and Bürgmann (2021; references therein). Additionally, Behr and Bürgmann (2021) in Figure 3 identify a depth range for deep ETS comprised between 0.7–1.7 GPa that is in perfect agreement with what we computed as P-T conditions of deformation in this study.

The peculiarity of the present case study is that in the Northern Apennines deep ETS are recorded in continental metasediments. A modern analogous to the Northern Apennines could be represented by the Taiwan orogenic system, where the Chinese continental margin experienced subduction to HP conditions below the Luzon Arc (Malavieille & Trullenque, 2009). HP units of Taiwan recorded metamorphic conditions of 1–1.2 GPa and  $\sim 550^{\circ}\text{C}$ , corresponding to depths of  $\sim 35$ –40 km, that were related to the transition from oceanic subduction to arc-continent collision (Beysac et al., 2008 and references therein). Therefore, Taiwan experienced higher geothermal gradient compared to the Northern Apennines (for the latter, see P-T of this study and summary of P-T data in Figure 1 of Bianco et al., 2019). Similarities between the Alps-Northern Apennines and Taiwan orogenic systems were recognised by Molli and Malavieille (2011). In particular, these authors proposed that the two orogenic systems share several similarities such as obliquity of convergence, opposite verging subduction, flip in subduction polarity with slab-breakoff and slab rollback with opening of back-arc basin (Figure 5 of Molli & Malavieille, 2011). Deep tremors are detected below the southern Central Range of Taiwan at depths between 15 and 45 km and are suggested to be associated to slow slips (Chen et al., 2018; Chuang et al., 2014; Ide et al., 2015). These authors related these phenomena to metamorphic dehydration reactions occurring within subducting continental crust producing high pore pressure and failure along low dipping thrust faults, similar to what is documented and proposed in this study for the Monticiano-Roccastrada Unit of the Northern Apennines.

## 6. Conclusions

We investigated a mesoscopic contractional structure developed at blueschist facies conditions in continental metasediments of the Northern Apennines (Italy). Field and microstructural analyses reveal a mylonitic foliation mutually overprinting with quartz and carpholite dilational hydroshear veins. Thermodynamic modeling constrains the formation of the mylonitic foliation to  $>0.7$  GPa and  $\sim 400^{\circ}\text{C}$  and the high-pressure vein at  $\sim 1.1$  GPa and  $\sim 350^{\circ}\text{C}$  for. Our results suggest a cyclic brittle-ductile behavior occurring at high-pressure conditions. This could potentially reflect the repeated alternation between aseismic creep and deep episodic tremor and slow slip events during contractional top-to-the-E-NE setting at blueschist facies conditions. Moreover, the aqueous fluid locally released by metamorphic dehydration reactions is proposed to be able to produce fluctuating pore pressure and to sustain brittle-ductile cyclicity, resulting in episodic tremor and slow slip events. To the best of our knowledge, this is the first time that brittle and ductile fabrics of a

mesoscopic contractional duplex are associated with deep episodic tremor and slow slip events. We suggest that fossil and exhumed geological records of deep episodic tremor and slow slip events are common at the scale of the entire Apennines belt, based on the widespread occurrence of quartz and carpholite dilatational hydroshear veins.

## Data Availability Statement

All data generated or analysed during this study are available within this published article, in its Supporting Information and in the Mendeley Data repository (<http://dx.doi.org/10.17632/mw7hwpgkc8.1>).

## Acknowledgments

The authors warmly acknowledge Stefano Poli and Andrea Risplendente for the acquisition of the EPMA data. Roberto Braga is thanked for fruitful discussion on thermodynamic modeling. They acknowledge thorough, constructive and helpful reviews from Giancarlo Molli, an anonymous reviewer and Enrico Tavarnelli. They are grateful to Whitney Behr for editorial handling. This project has received funding from the European Union's Horizon 2020 research and innovation programme under the Marie Skłodowska-Curie grant agreement No 839779. Open Access Funding provided by Università di Bologna within the CRUI-CARE Agreement.

## References

- Agard, P., Labrousse, L., Elvevold, S., & Lepvrier, C. (2005). Discovery of Paleozoic Fe-Mg carpholite in Motalafjella, Svalbard Caledonides: A milestone for subduction-zone gradients. *Geology*, 33(10), 761–764. <https://doi.org/10.1130/G21693.1>
- Airaghi, L., Lanari, P., de Sigoyer, J., & Guillot, S. (2017). Microstructural vs compositional preservation and pseudomorphic replacement of muscovite in deformed metapelites from the Longmen Shan (Sichuan, China). *Lithos*, 282–283, 262–280. <https://doi.org/10.1016/j.lithos.2017.03.013>
- Aldinucci, M., Brogi, A., & Spina, A. (2008). Middle-Late Permian sporomorphs from the Farma Formation (Monticiano-Roccastrada Ridge, southern Tuscany): New constraints for the tectono-sedimentary history of the Tuscan Domain. Stratigraphy and palaeogeography of late- and post-Hercynian Basins in the Southern Alps, Tuscany and Sardinia (Italy). *Italian Journal of Geosciences (Bollettino Della Società Geologica Italiana)*, 127(3), 581–597.
- Angiboust, S., Agard, P., Yamato, P., & Raimbourg, H. (2012). Eclogite breccias in a subducted ophiolite: A record of intermediate-depth earthquakes? *Geology*, 40(8), 707–710. <https://doi.org/10.1130/g32925.1>
- Angiboust, S., Kirsch, J., Oncken, O., Glodny, J., Monié, P., & Rybacki, E. (2015). Probing the transition between seismically coupled and decoupled segments along an ancient subduction interface. *Geochemistry, Geophysics, Geosystems*, 16(6), 1905–1922. <https://doi.org/10.1002/2015gc005776>
- Austrheim, H. (1987). Eclogitization of lower crustal granulites by fluid migration through shear zones. *Earth and Planetary Science Letters*, 81, 221–232. [https://doi.org/10.1016/0012-821X\(87\)90158-0](https://doi.org/10.1016/0012-821X(87)90158-0)
- Azzaro, E., Cocozza, T., Di Sabatino, B., Gasperi, G., Gelmini, R., Lazzarotto, A., et al. (1976). Geology and petrography of the Verrucano and Paleozoic formations of southern Tuscany and northern Latium (Italy). In H. Falke (Ed.), *The continental Permian in central, west, and south Europe* (pp. 181–195). Dordrecht: Springer Netherlands. [https://doi.org/10.1007/978-94-010-1461-8\\_15](https://doi.org/10.1007/978-94-010-1461-8_15)
- Barnes, P. M., Wallace, L. M., Saffer, D. M., Bell, R. E., Underwood, M. B., Fagereng, A., et al. (2020). Slow slip source characterized by lithological and geometric heterogeneity. *Science Advances*, 6(13), eaay3314. <https://doi.org/10.1126/sciadv.aay3314>
- Behr, W. M., & Bürgmann, R. (2021). What's down there? The structures, materials and environment of deep-seated slow slip and tremor. *Philosophical Transactions of the Royal Society A: Mathematical, Physical & Engineering Sciences*, 379(2193), 20200218. <https://doi.org/10.1098/rsta.2020.0218>
- Behr, W. M., Kotowski, A. J., & Ashley, K. T. (2018). Dehydration-induced rheological heterogeneity and the deep tremor source in warm subduction zones. *Geology*, 46(5), 475–478. <https://doi.org/10.1130/g40105.1>
- Berman, R. G. (1988). Internally consistent thermodynamic data for minerals in the system Na<sub>2</sub>O-K<sub>2</sub>O-CaO-MgO-FeO-Fe<sub>2</sub>O<sub>3</sub>-Al<sub>2</sub>O<sub>3</sub>-SiO<sub>2</sub>-TiO<sub>2</sub>-H<sub>2</sub>O-CO<sub>2</sub>. *Journal of Petrology*, 29(2), 445–522. <https://doi.org/10.1093/petrology/29.2.445>
- Bernaudin, M., & Gueydan, F. (2018). Episodic tremor and slip explained by fluid-enhanced microfracturing and sealing. *Geophysical Research Letters*, 45(8), 3471–3480. <https://doi.org/10.1029/2018GL077586>
- Beroza, G. C., & Ide, S. (2011). Slow earthquakes and nonvolcanic tremor. *Annual Review of Earth and Planetary Sciences*, 39(1), 271–296. <https://doi.org/10.1146/annurev-earth-040809-152531>
- Beysac, O., Negro, F., Simoes, M., Chan, Y.-C., & Chen, Y.-G. (2008). High-pressure metamorphism in Taiwan: From oceanic subduction to arc-continent collision? *Terra Nova*, 20(2), 118–125. <https://doi.org/10.1111/j.1365-3121.2008.00796.x>
- Bianco, C., Brogi, A., Caggianelli, A., Giorgetti, G., Liotta, D., & Meccheri, M. (2015). HP-LT metamorphism in Elba Island: Implications for the geodynamic evolution of the inner Northern Apennines (Italy). *Journal of Geodynamics*, 91, 13–25. <https://doi.org/10.1016/j.jog.2015.08.001>
- Bianco, C., Godard, G., Halton, A., Brogi, A., Liotta, D., & Caggianelli, A. (2019). The lawsonite-glaucophane blueschists of Elba Island (Italy). *Lithos*, 348, 105198. <https://doi.org/10.1016/j.lithos.2019.105198>
- Black, P. M., Maurizot, P., Ghent, E. D., & Stout, M. Z. (1993). Mg-Fe carpholites from aluminous schists in the Diahot region and implications for preservation of high-pressure/low-temperature schists, northern New Caledonia. *Journal of Metamorphic Geology*, 11(3), 455–460. <https://doi.org/10.1111/j.1525-1314.1993.tb00162.x>
- Bousquet, R., Oberhänsli, R., Goffé, B., Jolivet, L., & Vidal, O. (1998). High pressure-low temperature metamorphism and deformation in the “Bündnerschiefer” of the Engadine window (eastern Central Alps): Implications for regional evolution. *Journal of Metamorphic Geology*, 16, 653–674. <https://doi.org/10.1111/j.1525-1314.1998.00161.x>
- Brander, L., Svahnberg, H., & Piazzolo, S. (2012). Brittle-plastic deformation in initially dry rocks at fluid-present conditions: Transient behaviour of feldspar at mid-crustal levels. *Contributions to Mineralogy and Petrology*, 163(3), 403–425. <https://doi.org/10.1007/s00410-011-0677-5>
- Brogi, A., & Giorgetti, G. (2012). Tectono-metamorphic evolution of the siliciclastic units in the Middle Tuscan Range (inner Northern Apennines): Mg-carpholite bearing quartz veins related to syn-metamorphic syn-orogenic foliation. *Tectonophysics*, 526, 167–184. <https://doi.org/10.1016/j.tecto.2011.09.015>
- Brown, J. R., Beroza, G. C., Ide, S., Ohta, K., Shelly, D. R., Schwartz, S. Y., et al. (2009). Deep low-frequency earthquakes in tremor localize to the plate interface in multiple subduction zones. *Geophysical Research Letters*, 36(19). <https://doi.org/10.1029/2009gl040027>
- Bukovská, Z., Jeřábek, P., & Morales, L. F. G. (2016). Major softening at brittle-ductile transition due to interplay between chemical and deformation processes: An insight from evolution of shear bands in the South American Shear Zone. *Journal of Geophysical Research: Solid Earth*, 121(2), 1158–1182. <https://doi.org/10.1002/2015JB012319>

- Burgassi, P. D., PD, B., & Dell'Agnello, L. (1979). Esame dei rapporti fra le formazioni metamorfiche del basamento nella Toscana a Sud dell'Arno. *Memorie della Societa Geologica Italiana*, 20, 123–133.
- Capezuoli, E., Spina, A., Brogi, A., Liotta, D., Bagnoli, G., Zucchi, M., et al. (2021). Reconsidering the Variscan basement of southern Tuscany (inner Northern Apennines). *Geosciences*. <https://doi.org/10.3390/geosciences11020084>
- Capponi, G., Cortesogno, L., Crispini, L., Gaggero, L., & Giammarino, S. (1997). The promontorio del Franco (Island of Giglio): A blueschist element in the Tuscan archipelago (Central Italy). *Atti Ticinensi di Scienze della Terra*, 39, 175–192.
- Carmignani, L., Decandia, F. A., Fantozzi, P. L., Lazzarotto, A., Liotta, D., & Meccheri, M. (1994). Tertiary extensional tectonics in Tuscany (northern Apennines, Italy). *Tectonophysics*, 238(1–4), 295–315. [https://doi.org/10.1016/0040-1951\(94\)90061-2](https://doi.org/10.1016/0040-1951(94)90061-2)
- Carminati, E., & Doglioni, C. (2012). Alps vs. Apennines: The paradigm of a tectonically asymmetric Earth. *Earth-Science Reviews*, 112(1), 67–96. <https://doi.org/10.1016/j.earscirev.2012.02.004>
- Casini, G., Decandia, F. A., & Tavarnelli, E. (2007). Analysis of a mesoscopic duplex in SW Tuscany, Italy: Implications for thrust system development during positive tectonic inversion. *Geological Society, London, Special Publications*, 272(1), 437–446. <https://doi.org/10.1144/gsl.sp.2007.272.01.22>
- Casini, G., Decandia, F. A., & Tavarnelli, E. (2008). Pre-orogenic extensional deformations within Permian-Triassic rocks of Southern Tuscany: Structural record of an episode of Early Mesozoic continental rifting? *Bollettino della Societa Geologica Italiana*, 127(3), 615–624.
- Chen, K. H., Tai, H., Ide, S., Byrne, T. B., & Johnson, C. W. (2018). Tidal modulation and tectonic implications of tremors in Taiwan. *Journal of Geophysical Research: Solid Earth*, 123(7), 5945–5964. <https://doi.org/10.1029/2018jg015663>
- Chuang, L. Y., Chen, K. H., Wech, A., Byrne, T., & Peng, W. (2014). Ambient tremors in a collisional orogenic belt. *Geophysical Research Letters*, 41(5), 1485–1491. <https://doi.org/10.1002/2014gl059476>
- Compton, K. E., Kirkpatrick, J. D., & Holk, G. J. (2017). Cyclical shear fracture and viscous flow during transitional ductile-brittle deformation in the Saddlebag Lake Shear Zone, California. *Tectonophysics*, 708, 1–14. <https://doi.org/10.1016/j.tecto.2017.04.006>
- Condit, C. B., Guevara, V. E., Delph, J. R., & French, M. E. (2020). Slab dehydration in warm subduction zones at depths of episodic slip and tremor. *Earth and Planetary Science Letters*, 552, 116601. <https://doi.org/10.1016/j.epsl.2020.116601>
- Conti, P., Costantini, A., Tongiorgi, M., Di Pisa, A., & Decandia, F. A. (1991). Structural frame of the Tuscan Paleozoic: A review. *Bollettino della Societa Geologica Italiana*, 110(3–4), 523–541.
- Costantini, A., Decandia, F. A., Lazzarotto, A., & Sandrelli, F. (1988). L'unità di Monticiano-Roccastrada fra la Montagnola senese ed il Monte Leonì (Toscana meridionale). *Atti Ticinensi di Scienze della Terra*, 31, 382–420.
- Cox, S. F., & Etheridge, M. A. (1983). Crack-seal fibre growth mechanisms and their significance in the development of oriented layer silicate microstructures. *Tectonophysics*, 92(1–3), 147–170. [https://doi.org/10.1016/0040-1951\(83\)90088-4](https://doi.org/10.1016/0040-1951(83)90088-4)
- de Capitani, C., & Petrakakis, K. (2010). The computation of equilibrium assemblage diagrams with Theriak/Domino software. *American Mineralogist*, 95(7), 1006–1016. <https://doi.org/10.2138/am.2010.3354>
- Dragert, H., Wang, K., & James, T. S. (2001). A silent slip event on the deeper Cascadia subduction interface. *Science*, 292(5521), 1525–1528. <https://doi.org/10.1126/science.1060152>
- Droop, G. T. R. (1987). A general equation for estimating Fe<sup>3+</sup> concentrations in ferromagnesian silicates and oxides from microprobe analyses, using stoichiometric criteria. *Mineralogical Magazine*, 51(361), 431–435. <https://doi.org/10.1180/minmag.1987.051.361.10>
- El-Shazly, A. E. K. (1995). Petrology of Fe-Mg-carpholite-bearing metasediments from NE Oman. *Journal of Metamorphic Geology*, 13(3), 379–396. <https://doi.org/10.1111/j.1525-1314.1995.tb00227.x>
- Engi, M., Giuntoli, F., Lanari, P., Burn, M., Kunz, B., & Bouvier, A.-S. (2018). Pervasive eclogitization due to brittle deformation and rehydration of subducted basement: Effects on continental recycling? *Geochemistry, Geophysics, Geosystems*, 19(3), 865–881. <https://doi.org/10.1002/2017GC007215>
- Fagereng, Å., Hillary, G. W. B. B., & Diener, J. F. A. A. (2014). Brittle-viscous deformation, slow slip, and tremor. *Geophysical Research Letters*, 41(12), 4159–4167. <https://doi.org/10.1002/2014GL060433>
- Fagereng, Å., Remitti, F., & Sibson, R. H. (2010). Shear veins observed within anisotropic fabric at high angles to the maximum compressive stress. *Nature Geoscience*, 3(7), 482–485. <https://doi.org/10.1038/ngeo898>
- Fagereng, Å., Remitti, F., & Sibson, R. H. (2011). Incrementally developed slickenfibers: Geological record of repeating low stress-drop seismic events? *Tectonophysics*, 510(3), 381–386. <https://doi.org/10.1016/j.tecto.2011.08.015>
- Franceschelli, M., Leoni, L., Memmi, I., & Puxeddu, M. (1986). Regional distribution of Al-silicates and metamorphic zonation in the low-grade Verrucano metasediments from the northern Apennines, Italy. *Journal of Metamorphic Geology*, 4(3), 309–321. <https://doi.org/10.1111/j.1525-1314.1986.tb00353.x>
- Franceschelli, M., Memmi, I., Carcangiu, G., & Gianelli, G. (1997). Prograde and retrograde chloritoid zoning in low temperature metamorphism, Alpi Apuane, Italy. *Schweizerische Mineralogische Und Petrographische Mitteilungen*, 77, 41–50
- Gerald, J. D. F., & Stünitz, H. (1993). Deformation of granulitoids at low metamorphic grade. I: Reactions and grain size reduction. *Tectonophysics*, 221(3), 269–297. [https://doi.org/10.1016/0040-1951\(93\)90163-e](https://doi.org/10.1016/0040-1951(93)90163-e)
- Giorgetti, G., Goffe, B., Memmi, I., & Nieto, F. (1998). Metamorphic evolution of Verrucano metasediments in Northern Apennines; new petrological constraints. *European Journal of Mineralogy*, 10(6), 1295–1308. <https://doi.org/10.1127/ejm/10/6/1295>
- Giuntoli, F., Brovarone, A. V., & Menegon, L. (2020a). Feedback between high-pressure genesis of abiotic methane and strain localization in subducted carbonate rocks. *Scientific Reports*, 10(1), 9848. <https://doi.org/10.1038/s41598-020-66640-3>
- Giuntoli, F., & Engi, M. (2016). Internal geometry of the central Sesia Zone (Aosta Valley, Italy): HP tectonic assembly of continental slices. *Swiss Journal of Geosciences*, 109(3), 445–471. <https://doi.org/10.1007/s00015-016-0225-4>
- Giuntoli, F., Lanari, P., Burn, M., Eva Kunz, B., & Engi, M. (2018a). Deeply subducted continental fragments - Part 2: Insight from petrochronology in the central Sesia Zone (western Italian Alps). *Solid Earth*, 9(1). <https://doi.org/10.5194/se-9-191-2018>
- Giuntoli, F., Menegon, L., & Warren, C. J. (2018b). Replacement reactions and deformation by dissolution and precipitation processes in amphibolites. *Journal of Metamorphic Geology*, 36(9), 1263–1286. <https://doi.org/10.1111/jmg.12445>
- Giuntoli, F., Menegon, L., Warren, C. J., Darling, J., & Anderson, M. W. (2020b). Protracted shearing at midcrustal conditions during large-scale thrusting in the Scandinavian Caledonides. *Tectonics*, 39, e2020TC006267. <https://doi.org/10.1029/2020TC006267>
- Goffé, B., & Oberhänsli, R. (1992). Ferro- and magnesiocarpholite in the “Bündnerschiefer” of the eastern Central Alps (Grisons and Engadine Window). *European Journal of Mineralogy*, 4, 835–838. <https://doi.org/10.1127/ejm/4/4/0835>
- Gomberg, J., the Cascadia 2007, & Beyond Working Group (2010). Slow-slip phenomena in Cascadia from 2007 and beyond: A review. *The Geological Society of America Bulletin*, 122(7–8), 963–978. <https://doi.org/10.1130/b30287.1>
- Gueydan, F., Leroy, Y. M., Jolivet, L., & Agard, P. (2003). Analysis of continental midcrustal strain localization induced by microfracturing and reaction-softening. *Journal of Geophysical Research*, 108(B2). <https://doi.org/10.1029/2001jb000611>

- Hyndman, R. D. (1994). Widespread fluids in the lower crust: A source to crustal penetrating faults? In S. H. Hickman, R. H. Sibson, R. L. Bruhn, & et al. (Eds.), *Proceedings of workshop LXIII; USGS Red-book conference on the mechanical involvement of fluids in faulting* (pp. 178–188). Reston, VA: U. S. Geological Survey.
- Ide, S., Yabe, S., Tai, H.-J., & Chen, K. H. (2015). Thrust-type focal mechanisms of tectonic tremors in Taiwan: Evidence of subduction. *Geophysical Research Letters*, *42*(9), 3248–3256. <https://doi.org/10.1002/2015GL063794>
- Ito, Y., Obara, K., Shiomi, K., Sekine, S., & Hirose, H. (2007). Slow earthquakes coincident with episodic tremors and slow slip events. *Science*, *315*(5811), 503–506. <https://doi.org/10.1126/science.1134454>
- Jolivet, L., Faccenna, C., Goffé, B., Mattei, M., Rossetti, F., Brunet, C., et al. (1998). Midcrustal shear zones in postorogenic extension: Example from the northern Tyrrhenian Sea. *Journal of Geophysical Research*, *103*(B6), 12123–12160. <https://doi.org/10.1029/97jb03616>
- Keller, J. V. A., & Piali, G. (1990). Tectonics of the Island of Elba: A reappraisal. *Bollettino della Societa Geologica Italiana*, *109*(2), 413–425.
- Kirkpatrick, J. D., Fagereng, Å., & Shelly, D. R. (2021). Geological constraints on the mechanisms of slow earthquakes. *Nature Reviews Earth & Environment*. <https://doi.org/10.1038/s43017-021-00148-w>
- Koehn, D., & Passchier, C. W. (2000). Shear sense indicators in striped bedding-veins. *Journal of Structural Geology*, *22*(8), 1141–1151. [https://doi.org/10.1016/S0191-8141\(00\)00028-6](https://doi.org/10.1016/S0191-8141(00)00028-6)
- Kotowski, A. J., & Behr, W. M. (2019). Length scales and types of heterogeneities along the deep subduction interface: Insights from exhumed rocks on Syros Island, Greece. *Geosphere*, *15*(4), 1038–1065. <https://doi.org/10.1130/GES02037.1>
- Lanari, P., & Engi, M. (2017). Local bulk composition effects on metamorphic mineral assemblages. *Reviews in Mineralogy and Geochemistry*, *83*, 55–102. <https://doi.org/10.2138/rmg.2017.83.1>
- Lanari, P., Vidal, O., Lewin, E., Dubacq, B., De Andrade, V., & Schwartz, S. (2014). XMapTools a Matlab®-based graphic user interface for microprobe quantified image processing. *Computers & Geosciences*, *62*, 227–240. <https://doi.org/10.1016/j.cageo.2013.08.010>
- Lazzarotto, A., Aldinucci, M., Cirilli, S., Costantini, A., Decandia, F. A., Pandeli, E., et al. (2003). Stratigraphic correlation of the Upper Palaeozoic-Triassic successions in southern Tuscany, Italy. *Bollettino Della Societa Geologica Italiana, Special Volumes*, *2*, 25–35.
- Lo Pò, D., & Braga, R. (2014). Influence of ferric iron on phase equilibria in greenschist facies assemblages: The hematite-rich metasedimentary rocks from the Monti Pisani (Northern Apennines). *Journal of Metamorphic Geology*, *32*(4), 371–387. <https://doi.org/10.1111/jmg.12076>
- Malatesta, C., Federico, L., Crispini, L., & Capponi, G. (2018). Fluid-controlled deformation in blueschist-facies conditions: Plastic vs brittle behaviour in a brecciated mylonite (Voltri Massif, Western Alps, Italy). *Geological Magazine*, *155*(2), 335–355. <https://doi.org/10.1017/S0016756816001163>
- Malavieille, J., & Trullenque, G. (2009). Consequences of continental subduction on forearc basin and accretionary wedge deformation in SE Taiwan: Insights from analogue modeling. *Tectonophysics*, *466*(3–4), 377–394. <https://doi.org/10.1016/j.tecto.2007.11.016>
- Mancktelow, N. S., & Pennacchioni, G. (2005). The control of precursor brittle fracture and fluid-rock interaction on the development of single and paired ductile shear zones. *Journal of Structural Geology*, *27*(4), 645–661. <https://doi.org/10.1016/j.jsg.2004.12.001>
- Marchesini, B., Garofalo, P. S., Menegon, L., Mattila, J., & Viola, G. (2019). Fluid-mediated, brittle-ductile deformation at seismogenic depth—Part 1: Fluid record and deformation history of fault veins in a nuclear waste repository (Olkiluoto Island, Finland). *Solid Earth*, *10*(3), 809–838. <https://doi.org/10.5194/se-10-809-2019>
- Menegon, L., & Fagereng, Å. (2021). Tectonic pressure gradients during viscous creep drive fluid flow and brittle failure at the base of the seismogenic zone. *Geology*. <https://doi.org/10.1130/G49012.1>
- Menegon, L., Stünitz, H., Nasipuri, P., Heilbronner, R., & Svahnberg, H. (2013). Transition from fracturing to viscous flow in granulite facies perthitic feldspar (Lofoten, Norway). *Journal of Structural Geology*, *48*, 95–112. <https://doi.org/10.1016/j.jsg.2012.12.004>
- Molli, G. (2008). Northern Apennine-Corsica orogenic system: An updated overview. *Geological Society, London, Special Publications*, *298*(1), 413–442. <https://doi.org/10.1144/sp298.19>
- Molli, G., Brovarone, A. V., Beyssac, O., & Cinquini, I. (2018a). RSCM thermometry in the Alpi Apuane (NW Tuscany, Italy): New constraints for the metamorphic and tectonic history of the inner northern Apennines. *Journal of Structural Geology*, *113*, 200–216. <https://doi.org/10.1016/j.jsg.2018.05.020>
- Molli, G., Carlini, M., Vescovi, P., Artoni, A., Balsamo, F., Camurri, F., et al. (2018b). Neogene 3-D structural architecture of the north-west Apennines: The role of the low-angle normal faults and basement thrusts. *Tectonics*, *37*(7), 2165–2196. <https://doi.org/10.1029/2018tc005057>
- Molli, G., Giorgetti, G., & Meccheri, M. (2000). Structural and petrological constraints on the tectono-metamorphic evolution of the Massa Unit (Alpi Apuane, NW Tuscany, Italy). *Geological Journal*, *35*(3–4), 251–264. <https://doi.org/10.1002/gj.860>
- Molli, G., Giorgetti, G., & Meccheri, M. (2002). Tectono-metamorphic evolution of the Alpi Apuane metamorphic complex: New data and constraints for geodynamic models. *Bollettino della Societa Geologica Italiana*, *1*, 789–800.
- Molli, G., & Malavieille, J. (2011). Orogenic processes and the Corsica/Apennines geodynamic evolution: Insights from Taiwan. *International Journal of Earth Sciences*, *100*(5), 1207–1224. <https://doi.org/10.1007/s00531-010-0598-y>
- Molli, G., Menegon, L., & Malasoma, A. (2017). Switching deformation mode and mechanisms during subduction of continental crust: A case study from Alpine Corsica. *Solid Earth*, *8*(4), 767. <https://doi.org/10.5194/se-8-767-2017>
- Montomoli, C., Carosi, R., & Pertusati, P. C. (2009). Tectonic history of the Monti dell'Uccellina range, Southern Tuscany, Italy. *Bollettino della Societa Geologica Italiana*, *128*(2), 515–526. <https://doi.org/10.3301/ijg.2009.128.2.515>
- Muñoz-Montecinos, J., Angiboust, S., Cambeses, A., & Garcia-Casco, A. (2020). Multiple veining in a paleo-accretionary wedge: The metamorphic rock record of prograde dehydration and transient high pore-fluid pressures along the subduction interface (Western Series, central Chile). *Geosphere*, *16*(3), 765–786. <https://doi.org/10.1130/GES02227.1>
- Obara, K. (2002). Nonvolcanic deep tremor associated with subduction in southwest Japan. *Science*, *296*(5573), 1679–1681. <https://doi.org/10.1126/science.1070378>
- Ohlmacher, G. C., & Aydin, A. (1997). Mechanics of vein, fault and solution surface formation in the Appalachian Valley and Ridge, north-eastern Tennessee, USA: Implications for fault friction, state of stress and fluid pressure. *Journal of Structural Geology*, *19*(7), 927–944. [https://doi.org/10.1016/S0191-8141\(97\)00015-1](https://doi.org/10.1016/S0191-8141(97)00015-1)
- Papeschi, S., Musumeci, G., Massonne, H.-J., Mazzarini, F., Ryan, E. J., & Viola, G. (2020). High-P (P = 1.5–1.8 GPa) blueschist from Elba: Implications for underthrusting and exhumation of continental units in the Northern Apennines. *Journal of Metamorphic Geology*, *38*(5), 495–525. <https://doi.org/10.1111/jmg.12530>
- Peacock, S. M. (1990). Fluid processes in subduction zones. *Science*, *248*(4953), 329–337. <https://doi.org/10.1126/science.248.4953.329>
- Pertusati, P. C., Raggi, G., Ricci, C. A., Duranti, S., & Palmeri, R. (1993). Evoluzione post-collisionale dell'Elba centro-orientale. *Memorie della Societa Geologica Italiana*, *49*, 297–312.

- Platt, J. P., Xia, H., & Schmidt, W. L. (2018). Rheology and stress in subduction zones around the aseismic/seismic transition. *Progress in Earth and Planetary Science*, 5(1), 24. <https://doi.org/10.1186/s40645-018-0183-8>
- Pourteau, A., Bousquet, R., Vidal, O., Plunder, A., Duesterhoeft, E., Candan, O., & Oberhänsli, R. (2014). Multistage growth of Fe–Mg–carpholite and Fe–Mg–chloritoid, from field evidence to thermodynamic modelling. *Contributions to Mineralogy and Petrology*, 168(6), 1090. <https://doi.org/10.1007/s00410-014-1090-7>
- Prando, F., Menegon, L., Anderson, M., Marchesini, B., Mattila, J., & Viola, G. (2020). Fluid-mediated, brittle-ductile deformation at seismogenic depth-Part 2: Stress history and fluid pressure variations in a shear zone in a nuclear waste repository (Olkiluoto Island, Finland). *Solid Earth*, 11(2), 489–511. <https://doi.org/10.5194/se-11-489-2020>
- Putnis, A. (2015). Transient porosity resulting from fluid-mineral interaction and its consequences. *Reviews in Mineralogy and Geochemistry*, 80, 1–23. <https://doi.org/10.2138/rmg.2015.80.01>
- Putnis, A., & Putnis, C. V. (2007). The mechanism of reequilibration of solids in the presence of a fluid phase. *Journal of Solid State Chemistry*, 180(5), 1783–1786. <https://doi.org/10.1016/j.jssc.2007.03.023>
- Rau, A., & Tongiorgi, M. (1974). Geologia dei Monti Pisani a Sud-Est della Valle del Guappero. *Memorie della Societa Geologica Italiana*, 13, 227–408.
- Rimmelé, G., Oberhänsli, R., Goffé, B., Jolivet, L., Candan, O., & Çetinkaplan, M. (2003). First evidence of high-pressure metamorphism in the “Cover Series” of the southern Menderes Massif. Tectonic and metamorphic implications for the evolution of SW Turkey. *Lithos*, 71(1), 19–46. [https://doi.org/10.1016/S0024-4937\(03\)00089-6](https://doi.org/10.1016/S0024-4937(03)00089-6)
- Rossetti, F., Faccenna, C., Jolivet, L., Funicello, R., Goffé, B., Tecce, F., et al. (2001). Structural signature and exhumation PTt path of the Gorgona blueschist sequence (Tuscan archipelago, Italy). *Ophioliti*, 26(2a), 175–186.
- Rossetti, F., Faccenna, C., Jolivet, L., Funicello, R., Tecce, F., & Brunet, C. (1999). Syn-versus post-orogenic extension: The case study of Giglio Island (Northern Tyrrhenian Sea, Italy). *Tectonophysics*, 304(1–2), 71–93. [https://doi.org/10.1016/S0040-1951\(98\)00304-7](https://doi.org/10.1016/S0040-1951(98)00304-7)
- Ryan, E., Papeschi, S., Viola, G., Musumeci, G., Mazzarini, F., Torgersen, E., et al. (2021). Syn-orogenic exhumation of high-P units by upward extrusion in an accretionary wedge: Insights from the Eastern Elba nappe stack (Northern Apennines, Italy). *Tectonics*, 40(5), e2020TC006348. <https://doi.org/10.1029/2020TC006348>
- Saffer, D. M., & Tobin, H. J. (2011). Hydrogeology and mechanics of subduction zone forearcs: Fluid flow and pore pressure. *Annual Review of Earth and Planetary Sciences*, 39(1), 157–186. <https://doi.org/10.1146/annurev-earth-040610-133408>
- Shelly, D. R., Beroza, G. C., Ide, S., & Nakamura, S. (2006). Low-frequency earthquakes in Shikoku, Japan, and their relationship to episodic tremor and slip. *Nature*, 442(7099), 188–191. <https://doi.org/10.1038/nature04931>
- Simpson, C. (1986). Fabric development in brittle-to-ductile shear zones. *Pure and Applied Geophysics*, 124(1), 269–288. <https://doi.org/10.1007/bf00875728>
- Storti, F. (1995). Tectonics of the Punta Bianca promontory: Insights for the evolution of the Northern Apennines-Northern Tyrrhenian Sea basin. *Tectonics*, 14(4), 832–847. <https://doi.org/10.1029/95tc01203>
- Tarling, M. S., Smith, S. A. F. F., & Scott, J. M. (2019). Fluid overpressure from chemical reactions in serpentinite within the source region of deep episodic tremor. *Nature Geoscience*, 12(12), 1–9. <https://doi.org/10.1038/s41561-019-0470-z>
- Theye, T., Reinhardt, J., Goffé, B., Jolivet, L., & Brunet, C. (1997). Ferro- and magnesio-carpholite from the Monte Argentario (Italy): First evidence for high-pressure metamorphism of the metasedimentary Verrucano sequence, and significance for P-T path reconstruction. *European Journal of Mineralogy*, 9(4), 859–874. <https://doi.org/10.1127/ejm/9/4/0859>
- Torgersen, E., & Viola, G. (2014). Structural and temporal evolution of a reactivated brittle-ductile fault-Part I: Fault architecture, strain localization mechanisms and deformation history. *Earth and Planetary Science Letters*, 407, 205–220. <https://doi.org/10.1016/j.epsl.2014.09.019>
- Treppmann, C. A., & Seybold, L. (2019). Deformation at low and high stress-loading rates. *Geoscience Frontiers*, 10(1), 43–54. <https://doi.org/10.1016/j.gsf.2018.05.002>
- Ujiié, K., Saishu, H., Fagereng, Å., Nishiyama, N., Otsubo, M., Masuyama, H., & Kagi, H. (2018). An explanation of episodic tremor and slow slip constrained by crack-seal veins and viscous shear in subduction mélange. *Geophysical Research Letters*, 45(11), 5371–5379. <https://doi.org/10.1029/2018GL078374>
- Vignaroli, G., Faccenna, C., Rossetti, F., & Jolivet, L. (2009). Insights from the Apennines metamorphic complexes and their bearing on the kinematics evolution of the orogen. *Geological Society, London, Special Publications*, 311, 235–256. <https://doi.org/10.1144/sp311.9>
- Viola, G., Mancktelow, N. S., & Miller, J. A. (2006). Cyclic frictional-viscous slip oscillations along the base of an advancing nappe complex: Insights into brittle-ductile nappe emplacement mechanisms from the Naukluft Nappe Complex, central Namibia. *Tectonics*, 25(3). <https://doi.org/10.1029/2005TC001939>
- Viswanathan, K., & Seidel, E. (1979). Crystal chemistry of Fe–Mg–carpholites. *Contributions to Mineralogy and Petrology*, 70(1), 41–47. <https://doi.org/10.1007/bf00371870>
- Vitale, S., Fedele, L., Tramparulo, F. D., Ciarcia, S., Mazzoli, S., & Novellino, A. (2013). Structural and petrological analyses of the Frido Unit (southern Italy): New insights into the early tectonic evolution of the southern Apennines–Calabrian Arc system. *Lithos*, 168–169, 219–235. <https://doi.org/10.1016/j.lithos.2013.02.006>
- Wehrens, P., Berger, A., Peters, M., Spillmann, T., & Herwegh, M. (2016). Deformation at the frictional-viscous transition: Evidence for cycles of fluid-assisted embrittlement and ductile deformation in the granitoid crust. *Tectonophysics*, 693, 66–84. <https://doi.org/10.1016/j.tecto.2016.10.022>
- Whitney, D. L., & Evans, B. W. (2010). Abbreviations for names of rock-forming minerals. *American Mineralogist*, 95(1), 185–187. <https://doi.org/10.2138/am.2010.3371>